ARTICLES
https://doi.org/10.1038/s41590-019-0567-y

nature immunology

Corrected: Author Correction

The neuropeptide VIP confers anticipatory mucosal immunity by regulating ILC3 activity

Cyril Seillet[1,2*], Kylie Luong[1,2], Julie Tellier[1,2], Nicolas Jacquelot[1,2], Rui Dong Shen[1,2], Peter Hickey[1,2], Verena C. Wimmer[1,2], Lachlan Whitehead[1,2], Kelly Rogers[1,2], Gordon K. Smyth[1,3], Alexandra L. Garnham[1,2], Matthew E. Ritchie[1,2] and Gabrielle T. Belz[1,2,4*]

Group 3 innate lymphoid cell (ILC3)-mediated production of the cytokine interleukin-22 (IL-22) is critical for the maintenance of immune homeostasis in the gastrointestinal tract. Here, we find that the function of ILC3s is not constant across the day, but instead oscillates between active phases and resting phases. Coordinate responsiveness of ILC3s in the intestine depended on the food-induced expression of the neuropeptide vasoactive intestinal peptide (VIP). Intestinal ILC3s had high expression of the G protein-coupled receptor vasoactive intestinal peptide receptor 2 (VIPR2), and activation by VIP markedly enhanced the production of IL-22 and the barrier function of the epithelium. Conversely, deficiency in signaling through VIPR2 led to impaired production of IL-22 by ILC3s and increased susceptibility to inflammation-induced gut injury. Thus, intrinsic cellular rhythms acted in synergy with the cyclic patterns of food intake to drive the production of IL-22 and synchronize protection of the intestinal epithelium through a VIP–VIPR2 pathway in ILC3s.

The gut harbors trillions of symbiont, commensal and pathogenic bacteria[1] that have important positive or deleterious effects on immune function, nutrient processing and other host activities. Daily protection against this vast array of microorganisms depends on the enforced exclusion of potentially pathogenic microbes and harmful antigens derived from ingested material. Ingestion of food itself increases the possibility of encountering pathogens that could penetrate the epithelium to cause disease. The induction of immune-mediated repair mechanisms that maintain the integrity of the intestinal barrier is therefore essential to maintain homeostasis. Critical to this defense pathway is the ability to deal with the significant fluctuations that occur over time in the intestines[2]. Rhythmic cycles within cells provide a fundamental mechanism enabling the body to deal with diurnal changes in the intestinal environment, and allows the coordination of physiological processes with the induction of an immune response.

Innate lymphoid cells (ILCs)—particularly group 3 ILCs (ILC3s)—neutralize invasive pathogens at the intestinal epithelial surface to ensure maintenance of homeostasis[3,4]. ILC3-derived cytokines, such as interleukin-17 (IL-17), IL-22 and granulocyte–macrophage colony-stimulating factor, maintain immune homeostasis by triggering immune–epithelial signaling to modulate other immune cells, such as monocytes, which drive tissue repair programs[3,5]. IL-22 acts mainly on nonlymphoid cells, such as epithelial cells, and it is essential for maintenance of the barrier function and for tissue repair[6,7]. ILC3s are a major source of IL-22, which is required to protect against inflammatory damage induced by dextran sulfate sodium (DSS)[8] and bacterial infections such as *Clostridium difficile*[9] and *Citrobacter rodentium*[4,10–12]. Understanding the factors that modulate expression of IL-22 is of high importance for therapeutic approaches in inflammatory intestinal diseases[13,14]. In contrast with the positive functions of IL-22 in tissue repair, continuous exacerbated or uncontrolled activation of the IL-22 pathway, particularly in ILC3s, leads to increased intestinal permeability[15], chronic inflammation and increased risk of inflammatory bowel disease[16], Crohn's disease[17] and colitis-associated cancer[18], indicating a requirement for tight regulation of IL-22 signaling in the mucosal epithelium. The mechanims that normally restrain the overproduction of IL-22 during continual antigenic exposure remain unclear.

Transcriptomic analyses have shown that ILCs express a large array of receptors involved in the recognition of neuropeptides, hormones and metabolic signals[19,20]. These receptors allow immune cells to act as a rheostat and integrate diverse extrinsic and intrinsic signals to finely tune immune responses[20]. Hormone receptors such as the androgen receptor, expressed by ILC2s, protect against the development of experimental asthma in male mice[21], while the glucocorticoid receptor found on natural killer (NK) cells and ILC1s is triggered by lipopolysaccharide to downregulate the production of interferon-γ (IFN-γ) and confer protection against septic shock[22]. A variety of other receptors, including the neuroreceptors vasoactive intestinal peptide receptors 1 and 2 (VIPR1 and VIPR2, respectively)[23], neuromedin U receptor 1 (refs. [24–26]) and RET[8], are also expressed by ILC2s and ILC3s. These receptors have tissue-specific functions in the lung, indicating that ILCs integrate their responses in the context of their environment. This is especially important for ILCs, which respond to stimulation with rapid secretion of effector cytokines to mobilize early immune responses[27]. In addition, ILCs constitutively secrete mediators that are important for the homeostasis of mucosal tissues[28]. Nevertheless, disruption of the communication between ILCs and the neuronal and endocrinal pathways leads to altered immune responses with harmful consequences for the organism[3].

In the present study, we show that daily patterns of food intake coordinately regulated the responsiveness of ILC3s. This cyclicity was only partially controlled by circadian genes. Instead, food intake stimulated the release of the neuronal-derived signaling

[1]Walter and Eliza Hall Institute of Medical Research, Melbourne, Victoria, Australia. [2]Department of Medical Biology, University of Melbourne, Melbourne, Victoria, Australia. [3]School of Mathematics and Statistics, University of Melbourne, Melbourne, Victoria, Australia. [4]The University of Queensland Diamantina Institute, The University of Queensland, Brisbane, Queensland, Australia. *e-mail: seillet@wehi.edu.au; belz@wehi.edu.au

mediator VIP, which directly activated the expression of IL-22 in ILC3s through the neuroreceptor VIPR2. The number of enteric neurons that produced VIP was increased after feeding, which created a rhythmic pattern of VIP expression in the gut. Collectively, we describe a mechanism of temporal regulation of the ILC3 function in order to enforce innate defense and confer physiological protection of the gut coordinated with food intake.

Results

Cytokine production of ILCs oscillates throughout the day. Epithelial cells exhibit transcriptionally regulated diurnal fluctuations that allow temporal regulation of epithelial integrity[29]. To investigate whether the transcriptome and function of ILCs in the gastrointestinal tract were regulated in a cyclic manner, C57BL/6 mice were housed under strict 24 h dark–light cycles (lights on for 12 h, with the time of light onset denoted as t_0) and were fed ad libitum. The ability of ILCs and other lymphocytes isolated from the small intestine, lungs and mesenteric lymph node to produce cytokines at t_4 (4 h after light onset) and t_{16} (4 h after light offset) was determined after stimulating the cells ex vivo with phorbol-12-myristate-13-acetate (PMA) and ionomycin for 4.5 h. Intracellular expression of the cytokine tumor necrosis factor (TNF) was increased in lung NK1.1$^+$NKp46$^+$Eomes$^-$CD49a$^+$ ILC1s (identified as such throughout, unless otherwise specified) at t_4 compared with t_{16} (Extended Data Fig. 1a), while expression of IFN-γ and TNF in gut or mesenteric lymph node NK1.1$^+$NKp46$^+$Eomes$^+$CD49b$^+$NK cells and ILC1s was not significantly different between the two time points (Fig. 1a and Extended Data Fig. 1b). Expression of IL-5 by Lin$^-$Gata3$^+$Rorγt$^-$ ILC2s (identified as such throughout, unless otherwise specified) in the small intestine and lungs was significantly higher at t_{16} compared with t_4 (Fig. 1a and Extended Data Figs. 1 and 2). Production of IL-22, but not IL-17, was increased at t_{16} compared with t_4 in Lin$^-$Gata3$^-$Rorγt$^+$NKp46$^{+/-}$ ILC3s (identified as such throughout, unless otherwise specified) in the intestine, but not in the mesenteric lymph node or the lungs (Fig. 1a and Extended Data Figs. 1 and 2). CD4$^+$ T cells did not show changes in the expression of IFN-γ, TNF or IL-22 between t_4 and t_{16}, while expression of IL-17 in CD4$^+$ T cells showed rhythmicity, as previously observed[30] (Extended Data Fig. 3a,b). These data suggested that, among lymphocytes, ILC2s and ILC3s were particularly sensitive to temporal regulation.

To better understand the nature of the variation in the production of IL-5 and IL-22, we analyzed the ex vivo expression of these cytokines without further stimulation in ILC2s and ILC3s in the small intestine and lungs at t_4, t_{10}, t_{16} and t_{23}. Production of IL-5 by ILC2s in both tissues and IL-22 by ILC3s in the small intestine had a circadian pattern, with a peak at t_{12}–t_{16} and a nadir at t_{23}–t_4 (Fig. 1b), supporting previous reports of cyclic expression of IL-5 by ILC2s during the day[23]. To explore the mechanisms controlling the rhythmic expression of IL-22 in intestinal ILCs, we performed RNA sequencing (RNA–Seq) analyses on Lin$^-$CD45$^+$IL-7R$^+$CD90$^+$Sca1$^+$ ILC2s and Lin$^-$CD45$^+$IL-7R$^+$CD90$^+$CD117$^+$ ILC3s flow-purified from the small intestines of C57BL/6 mice at t_4, t_{10}, t_{16} and t_{23}. The ILC2 and ILC3 datasets were combined to define the core set of genes that oscillated in both types of cell. Rhythmic changes in gene expression across the four time points were identified using a single harmonic sinusoidal model (false discovery rate-adjusted $P < 0.05$). This analysis showed enrichment of genes involved in regulation of the circadian rhythm (*Dpb*, *Per1*, *Per2*, *Per3*, *Nr1d1*, *Nr1d2* and *Cry1*) (Fig. 1c), indicating that ILC2s and ILC3s express a functional molecular machinery for circadian rhythms. Three of the top 15 pathways identified using reactome analyses in ILC2s and ILC3s were related to circadian rhythms (Fig. 1d). Reactome analysis indicated that genes known to be regulated by the SMAD family (which acts as signal transducer for receptors of the transforming growth factor-β superfamily) and genes in the transforming growth factor-β signaling pathway (*Socs1*, *Ncor2* and *Trim33*) were upregulated at t_4 and t_{10} compared with other time points (Fig. 1c). Genes involved in metabolism—in particular, those transcribing enzymes involved in cholesterol biosynthesis, such as *Msmo1*, *Mvk*, *Nsdhl*, *Idi1*, *Fdps* and *Sqle*—were also increased at t_{23} compared with t_4–t_{16} (Fig. 1c). As such, ILCs exhibited significant cyclicity in gene regulation, especially among genes central to immune protection in the gut mucosa.

Intrinsic clock genes partly regulate cytokines in ILCs. To understand how the rhythmicity in ILC function was regulated, we examined the contribution of the circadian clock gene *Arntl*, which plays a key role in regulating oscillatory production of proteins, particularly cytokines[31]. Aryl hydrocarbon receptor nuclear translocator-like protein 1 (ARNTL) binds to DNA rhythmically to activate the expression of core clock genes[2]. Equal mixes of bone marrow cells from wild-type and *Il7rCre*×*Arntl*$^{fl/fl}$ mice (hereafter referred to as *Arntl*$^{\Delta IL7R}$), which have a conditional deletion of *Arntl* in all lymphoid lineages (data not shown), were injected into lethally irradiated wild-type recipients. Both wild-type and *Arntl*$^{\Delta IL7R}$ cells generated T cells, B cells and innate lymphoid subsets in the small intestine at 8 weeks post-transfer (Fig. 2a and Extended Data Fig. 4). However, the frequency and number of *Arntl*$^{\Delta IL7R}$ Rorγt$^+$ ILC3s were significantly diminished compared with the wild type (Fig. 2a,b and Extended Data Fig. 4). Intracellular staining showed a significant reduction of IL-22 in *Arntl*$^{\Delta IL7R}$ ILC3s compared with wild-type ILC3s, both constitutively and in response to IL-7 and IL-23 (Fig. 2c), consistent with previous reports[32]. In addition, purified enteric Lin$^-$CD45$^+$CD127$^+$CD90$^+$CD117$^+$ ILC3s from *Arntl*$^{\Delta IL7R}$ mice produced less IL-22 compared with wild-type ILC3s after stimulation with IL-7 or IL-7 + IL-23 (Fig. 2d and Extended Data Fig. 5), indicating that ARNTL was required for the optimal secretion of IL-22. Intracellular staining for IL-22 revealed that enteric *Arntl*$^{\Delta IL7R}$ ILC3s had increased production of IL-22 at t_{16} compared with t_4 (Fig. 2e), even though the amplitude of the oscillations was reduced relative to that observed in wild-type ILC3s (Fig. 2e). The reduction in the amplitude of the oscillations in ILC3s did not reach statistical significance (Fig. 2e). Addition of IL-23 to *Arntl*$^{\Delta IL7R}$ ILC3s did not restore the production of IL-22 to levels observed in wild-type ILC3s, while the oscillations in cytokine production were preserved (Fig. 2e). The overall production of IL-5, or the oscillatory pattern of IL-5 production, were similar in ILC2s from the lungs of wild-type and *Arntl*$^{\Delta IL7R}$ mice at t_4 and t_{16} (Fig. 2f). These observations suggested that ARNTL was important for the basal expression of IL-22, but it only partially controlled the rhythmic production of IL-22 in ILC3s.

Caloric intake is synchronized with ILC rhythmicity. Next, we investigated whether the rhythmic production of IL-22 in enteric ILC3s was regulated by extrinsic factors. First, we tracked mouse food consumption across the 24 h light–dark cycle. Food intake by mice was rhythmic, with maximum food intake during the dark phase (t_{12}–t_{24}) and less food intake during the light phase (t_0–t_{12}) (Fig. 3a). To test whether food intake influenced cytokine production in ILCs, food was provided only during the dark phase (t_{12}–t_{24}) or the light phase (t_0–t_{12}) for 7 d. The restriction in food availability across this time frame was not sufficient to change the active–rest cycle in mice[33]. On day 8, analysis of enteric ILCs at t_4 indicated that the frequency of ILC2s and ILC3s that constitutively produced IL-5 and IL-22, respectively, was almost twofold higher in mice fed during the dark phase (t_{12}–t_{24}) compared with mice fed during the light phase (t_0–t_{12}) (Fig. 3b,c). ILCs isolated from the lungs or the mesenteric lymph node did not show any significant change in IL-5 production between the two time points (Fig. 3b,c), suggesting that food intake modulated cytokine production in ILCs only in the intestines. Similarly, we did not observed differences in the production of cytokines in CD4$^+$ T cells in the small intestine (data

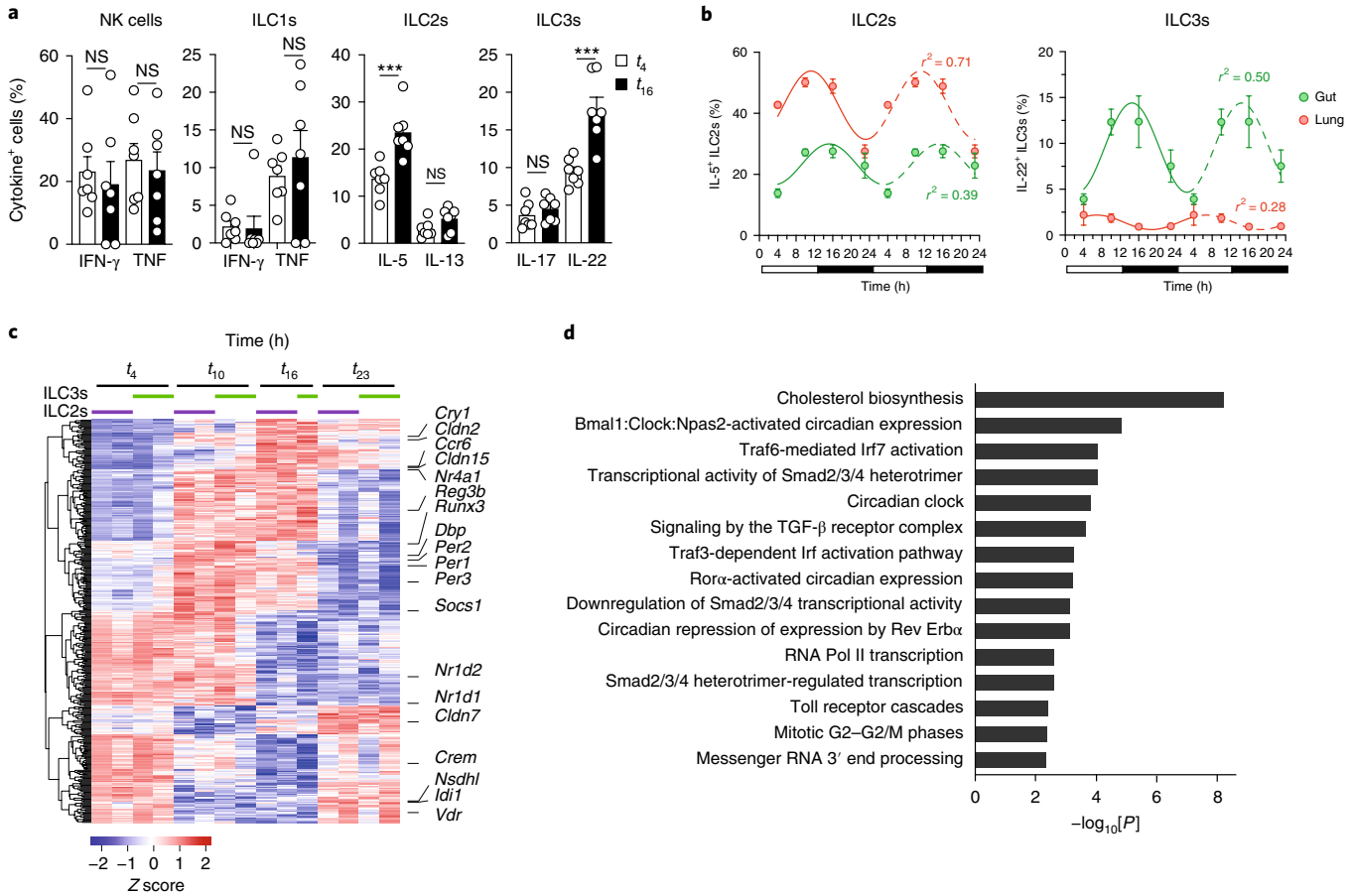

Fig. 1 | ILC2 and ILC3 activities oscillate during the active and resting phase at steady state in wild-type mice. a, Frequency of natural killer cells (Lin$^-$NK1.1$^+$NKp46$^+$Eomes$^+$CD49b$^+$), and ILC1s (Lin$^-$NK1.1$^+$NKp46$^+$Eomes$^-$CD49a$^+$) expressing IFN-γ or TNF, ILC2s (Lin$^-$Gata3$^+$Rorγt$^-$) expressing IL-5 or IL-13, and ILC3s (Lin$^-$Gata3$^+$Rorγt$^-$) expressing IL-17 or IL-22, isolated from the small intestine of wild-type mice at t_4 and t_{16} and stimulated in vitro for 4.5 h with PMA and ionomycin. Individual responses, together with means ± s.e.m., are shown ($n = 7$ mice per time point). One experiment representative of five independent experiments with similar results is shown. Statistical significance was determined using a two-tailed unpaired Student's *t*-test (***$P < 0.001$). NS, not significant. **b**, Frequency of IL-5 and IL-22 constitutively produced by ILC2s (left) and ILC3s (right), respectively, from the lung and small intestine at t_4, t_{10}, t_{16} and t_{23}. Solid lines represent cosinor regression and show the coefficient of determination (r^2). Dotted lines project duplicated data to better appreciate the circadian pattern. Data show means ± s.e.m. ($n = 6$ mice at t_4, t_{10} and t_{23}, and $n = 4$ mice at t_{16}) for one of two independent experiments. **c**,**d**, RNA–Seq analyses of ILC2s and ILC3s in the small intestine. The heatmap (**c**) depicts the common genes that follow a circadian pattern in combined ILC2s and ILC3s that were identified by expression of a periodic signal using a single harmonic sinusoidal model. Individual biological replicates are shown. In **d**, the top 15 pathways that oscillate are listed. These were identified in ILC2s and ILC3s using Reactome analyses (https://reactome.org/).

not shown), indicating that the 7-d controlled-food intake did not impact the cytokine secretion of other lymphocytes.

To test whether the microbiota could be responsible for the increased frequency of ILCs producing cytokines following food restriction, wild-type mice fed only during the dark (t_{12}–t_{24}) or light (t_0–t_{12}) phase were treated continuously with antibiotics in their drinking water for 2 weeks. Control mice were not treated with antibiotics and received food ad libitum. The antibiotic treatment did not alter the production of IL-22 in ILC3s isolated from mice fed during the dark phase (t_{12}–t_{24}) compared with the control group (Fig. 3e). Whether the mice were treated with antibiotics or not, we observed an increase of around twofold in the frequency of IL-22$^+$ ILC3s in mice fed during the dark phase (t_{12}–t_{24}) compared with the mice fed during the light phase (t_0–t_{12}; Fig. 3d), indicating that the increased production of IL-22 in ILC3s from mice fed during the dark phase (t_{12}–t_{24}) was independent of the microbiota. Next, we fasted the mice for 16 h (between t_{12} on day 0 and t_4 on day 1) and compared the ILC response to mice fed ad libitum. Analyses at t_4 on day 1 showed that ILC2s and ILC3s within the total small intestinal immune cells from fasted mice had a reduced expression of IL-5 (Fig. 3e) and IL-22 (Fig. 3f), respectively, when assessed constitutively or in the presence of IL-7 and IL-23, compared with fed mice. Cytokine production in ILCs from the mesenteric lymph node was not different between fed and fasted mice (Fig. 3e,f). Similarly, flow cytometrically purified enteric ILC3s from fasted mice showed a reduction in IL-22 compared with fed mice (Fig. 3g), indicating that the capacity of ILC3s to produce IL-22 constitutively or in response to IL-23 was imprinted in vivo. These observations suggested that an extrinsic signal linked to food consumption was responsible for the local modulation of IL-22 production in ILC3s in the small intestine, while ILC3s in the draining lymph node or lungs were not affected.

Intestinal ILC3s express the neuropeptide receptor VIPR2. To elucidate the mechanisms that controlled the tissue-specific regulatory program observed in enteric ILCs, we performed single-cell RNA–Seq on Lin$^-$CD127$^+$CD90$^+$ ILCs sorted at t_4 from the small intestine and the colon of wild-type mice kept on a 12 h light/12 h dark cycle and fed ad libitum. Data analysis using t-distributed stochastic neighbor embedding (t-SNE)[34] distinguished eight distinct

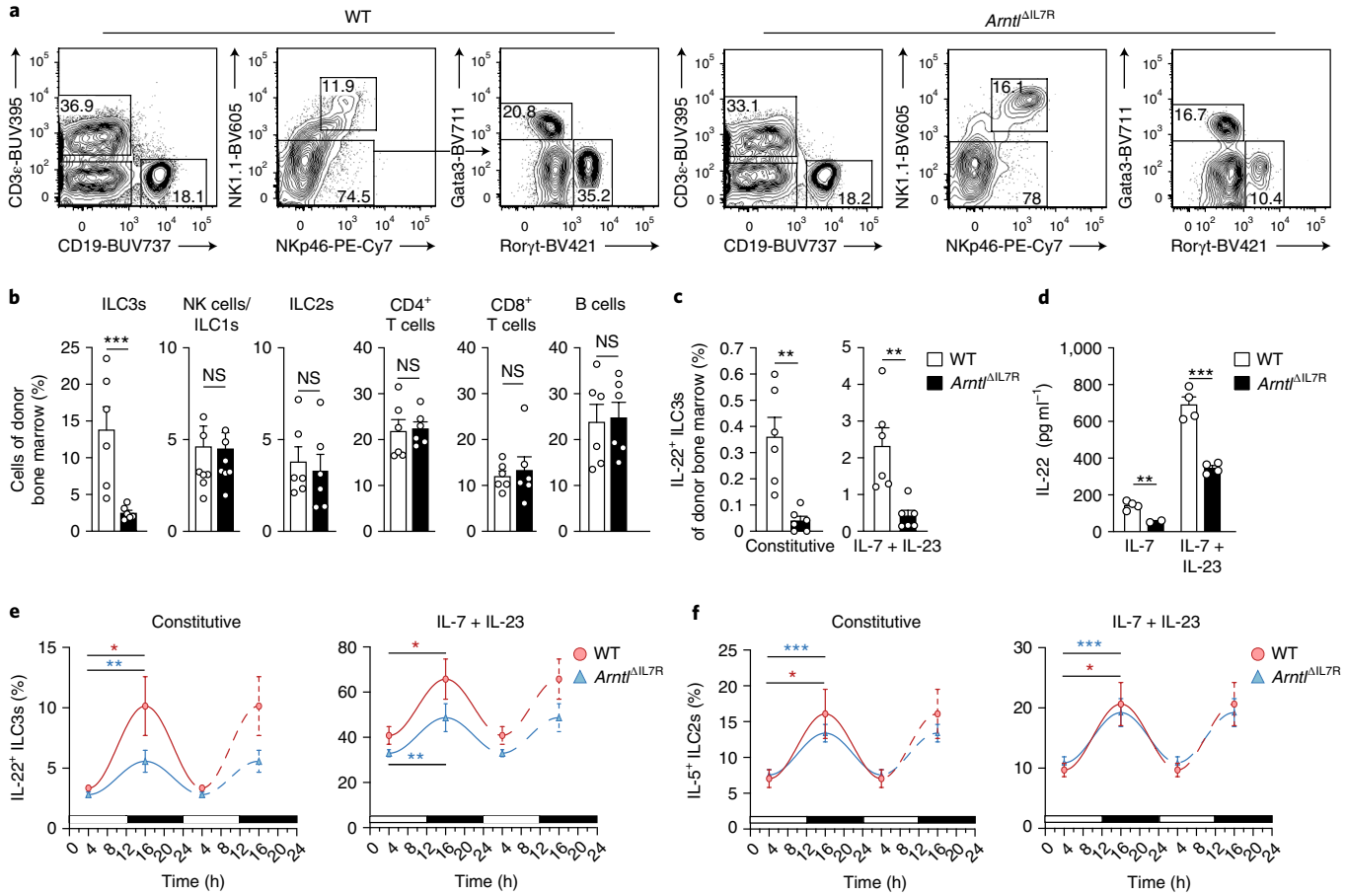

Fig. 2 | The molecular clock only partially regulates circadian expression of cytokine secretion. a–c, Mixed bone marrow chimeras were generated by reconstituting CD45.1$^{+/+}$ lethally irradiated recipients with F1 wild-type (WT) and CD45.2$^{+/+}$ *Arntl*$^{\Delta IL7R}$ bone marrow. **a**, Representative contour plots of the different enteric lymphocyte subsets of mixed bone marrow chimeras. Plots show live cells from wild-type or *Arntl*-deficient cells. Data are representative of one of three independent experiments. **b**, Frequency of different enteric lymphocyte subsets derived from wild-type (white bars) or *Arntl*-deficient donor bone marrow (black bars). **c**, Frequency of IL-22-producing enteric ILC3s among wild-type and *Arntl*-deficient cells. Data in **b** and **c** show means ± s.e.m. ($n = 6$ mice per experiment). **d**, A total of 4×10^3 ILC3s were purified from the small intestines of wild-type or *Arntl*$^{\Delta IL7R}$ mice and cultivated for 16 h in the presence of either recombinant IL-7 (10 ng ml^{-1}) or IL-7 together with IL-23 (10 ng ml^{-1}). IL-22 production was determined in culture supernatants by enzyme-linked immunosorbent assay (ELISA). Data are pooled from two independent experiments and show means ± s.e.m. ($n = 4$ mice). **e**,**f**, Frequency of IL-22- and IL-5-producing small intestinal ILC3s (**e**) and lung ILC2s (**f**), respectively, at t_4 and t_{16} that were isolated from wild-type and *Arntl*$^{\Delta IL7R}$ mice. Data show means ± s.e.m. of one of two similar experiments ($n = 4$ mice per genotype per time point per experiment). Solid lines show cosinor regression, while dotted lines project duplicated data. In **b**–**f**, statistical significance was determined by two-tailed unpaired Student's *t*-test (*$P < 0.05$; **$P < 0.01$; ***$P < 0.001$).

clusters in the small intestine, including: ILC1s and natural killer cells, which clustered together (cluster 7), ILC2s (cluster 4) and four subsets of ILC3s (clusters 1, 2, 3 and 6) (Fig. 4a). ILC3s in cluster 6 expressed the neuroendocrine receptor genes *Vipr2* (encoding VIPR2), *Ccr6* and *Cd4*, but were negative for *Ncr1* and *Tbx21* (Fig. 4b,c). While ILC3s in clusters 1 and 2 constitutively expressed *Csf2* and *Il2*, the *Vipr2*$^+$ ILC3s (cluster 6) mainly expressed *Il22* and *Il17* (Fig. 4c). In the colon, we also identified eight clusters (Extended Data Fig. 6a), but only one cluster of ILC3s (cluster 4) constitutively expressed *Il22*, along with *Ccr6* and *Cd4*. Some cells in cluster 4 expressed *Vipr2* (Extended Data Fig. 6b,c).

VIPR2 is a receptor for VIP—a neuropeptide that controls cellular rhythms[35–37]. VIP is expressed in intestinal neurons where it controls food intake and glucose metabolism[38], and was also reported to drive the production of IL-5 in ILC2s[23]. To investigate whether expression of VIPR2 in ILC3s coordinated the immune responsiveness of ILCs with the intake of food, we used confocal and light-sheet imaging of whole gut sections to examine the localization of VIP$^+$ neurons in the small intestine. An extensive network of β3-tubulin$^+$ neurons was detected from the base of the intestinal crypts into the villus within the submucosa and adjacent to the lacteals (Fig. 4d,e and Supplementary Video 1), and these β3-tubulin$^+$ neurons co-stained with VIP (Fig. 4d,e). In the small intestine and colon of *Rorc(γt)*$^{GFP/+}$ mice, in which GFP is expressed in the Rorγ locus and marks the ILC3s, staining for β3-tubulin$^+$ and VIP indicated that Rorγt-GFP$^+$CD3ε$^-$ ILC3s were located close to the VIP$^+$ neurons (Fig. 4f and Extended Data Fig. 6d). Next, we stained sections of the small intestine and colon isolated from wild-type mice fed ad libitum, and calculated the colocalization of the VIP stain with the β3-tubulin$^+$ neuronal axons at t_4 and t_{16}. The colocalization of VIP with the β3-tubulin$^+$ neurons was higher at t_{16} compared with t_4 in both the small intestine and colon (Fig. 4g and Extended Data Fig. 6e), indicating that VIP expression in the gut of mice was increased during the night (t_{16}). To investigate whether food intake was synchronized with the expression of VIP, we assessed VIP staining in the small intestine of wild-type mice fed ad libitum and in mice fasted for 16 h before analysis at t_4. The colocalization of β3-tubulin$^+$ with VIP in the small intestine was increased twofold

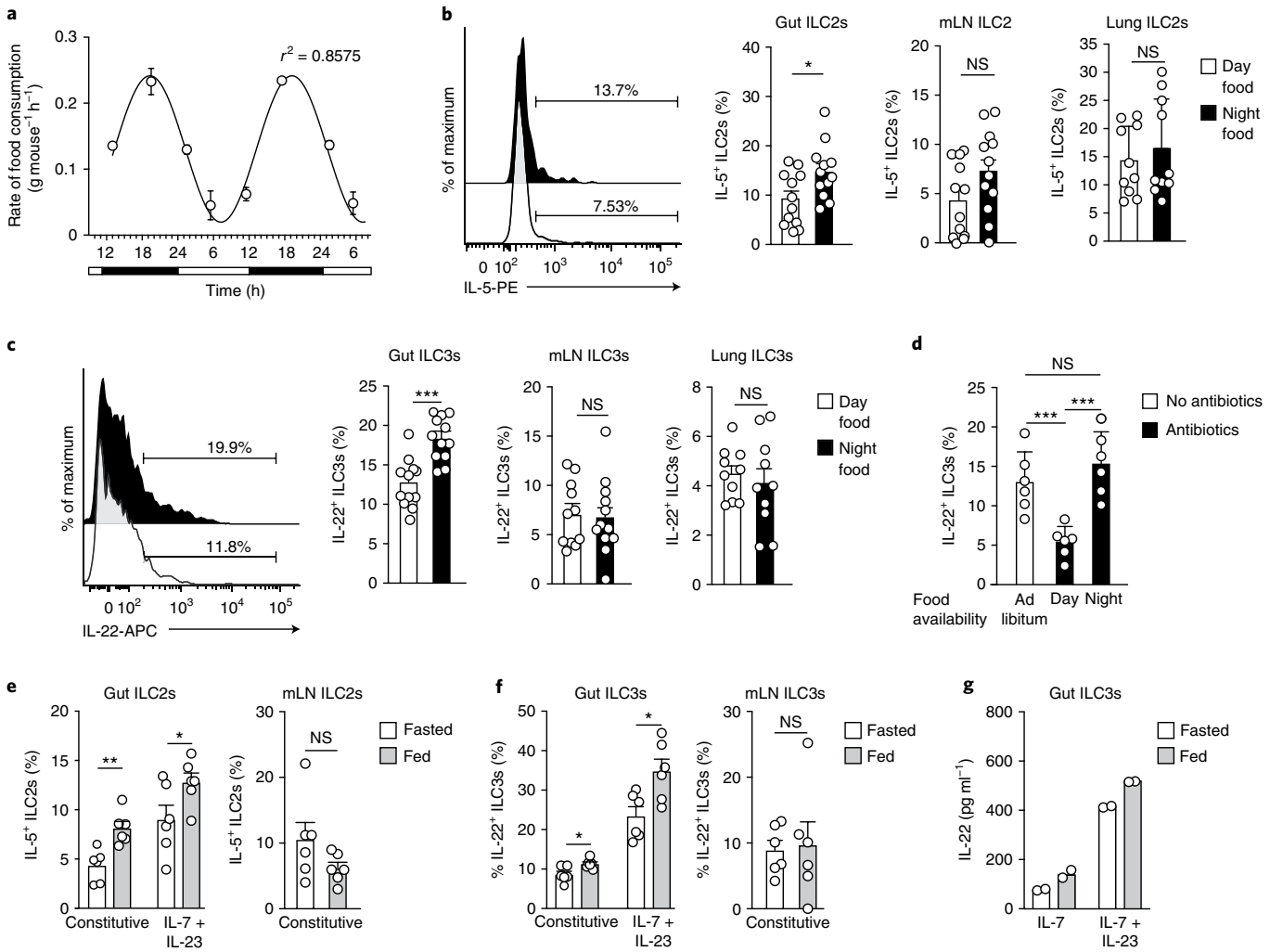

Fig. 3 | Food intake regulates the cytokine secretion of enteric ILC2s and ILC3s. a, Food consumption of mice was determined at the indicated time points ($n = 12$ mice per experiment). The line represents cosinor regression and shows the coefficient of determination (r^2). **b**,**c**, Left: Intracellular expression of IL-5$^+$ ILC2s (**b**) and IL-22$^+$ ILC3s (**c**). Right: frequency of constitutive IL-5$^+$ ILC2s (**b**) and IL-22$^+$ ILC3s (**c**) from the indicated tissues of mice fed only during the day or during the night. Data were pooled from two of four similar experiments (gut and mesenteric lymph node (mLN): $n = 12$ and 6 mice per experiment; lung: $n = 10$ and 5 mice per experiment). **d**, Mice were treated with antibiotics for 2 weeks before analysis of constitutive IL-22 production by intracellular staining ($n = 6$ mice per experimental condition). Data are representative of two independent experiments. **e**,**f**, Frequency of IL-5$^+$ ILC2s (**e**) and IL-22$^+$ ILC3s (**f**) from the small intestines and mesenteric lymph nodes of mice fasted for 16 h or fed ad libitum. Data are representative of three independent experiments ($n = 6$ mice per group per condition). **g**, Enteric ILC3s (7.5×10^3) were purified from fasted mice or mice fed ad libitum and cultivated for 16 h in the presence of IL-7 or IL-7 plus IL-23. IL-22 was determined in the culture supernatants by ELISA ($n = 2$ biological samples). Each circle represents ILC3s sorted from a pool of three mice per group. Data are pooled from two independent experiments. In **b**–**f**, data show means ± s.e.m., and statistical significance was determined by two-tailed unpaired Student's *t*-test (*$P < 0.05$; **$P < 0.01$; ***$P < 0.001$).

in fed mice compared with fasted mice (Fig. 4h), indicating that fasted mice had reduced expression of VIP in the enteric neurons. Thus, ILC3s in the intestine express VIPR2 and are located close to VIP$^+$ neurons, which increased in frequency after food intake and decreased after fasting.

Feeding coordinates the production of IL-22 in ILC3s. To assess whether exposure to VIP modulated the cytokine production in ILC3s, we stimulated CD45$^+$ lymphocytes isolated from the lamina propria of wild-type mice fasted for 16 h with IL-7 and IL-23 in the presence or absence of VIP for 4.5 h. Dibutyryl cyclic-AMP (d-cAMP), which mimics the direct stimulation with cAMP and activates protein kinases[39], was used as a positive control to bypass VIPR2 engagement. Enteric ILC3s from fasted mice stimulated for 4 h with synthetic VIP or d-cAMP had higher expression of intracellular IL-22 compared with ILC3s cultured with vehicle (Fig. 5a). To assess whether the enhancing effect of VIP on IL-22 expression in ILC3s in vitro could also be observed in fed mice, we purified ILC3s from mice fed ad libitum and incubated them with VIP for 16 h. VIP-stimulated ILC3s had higher production of IL-22 compared with control ILC3s, while addition of IL-23 amplified this effect even further (Fig. 5b). VIP and d-cAMP increased the expression of IL-22 in ILC3 in a dose-dependent manner (Fig. 5c,d) in both the constitutive and IL-23 + IL-7-induced conditions (Fig. 5c,d). The VIPR2 agonist BAY 55-9837 induced a similar increase in the production of IL-22 in purified ILC3s as VIP did (Fig. 5e), while the VIPR2 antagonist PG99-465 largely blocked VIP-induced expression of IL-22 secretion in ILC3s (Fig. 5f). These findings indicate that in vitro VIP signaling could enhance the production of IL-22 through the direct activation of VIPR2 on ILC3s.

Next, we injected VIP or phosphate buffered saline (PBS) intraperitoneally into wild-type mice and analyzed the Lin$^-$Gata3$^+$Rorγt$^-$

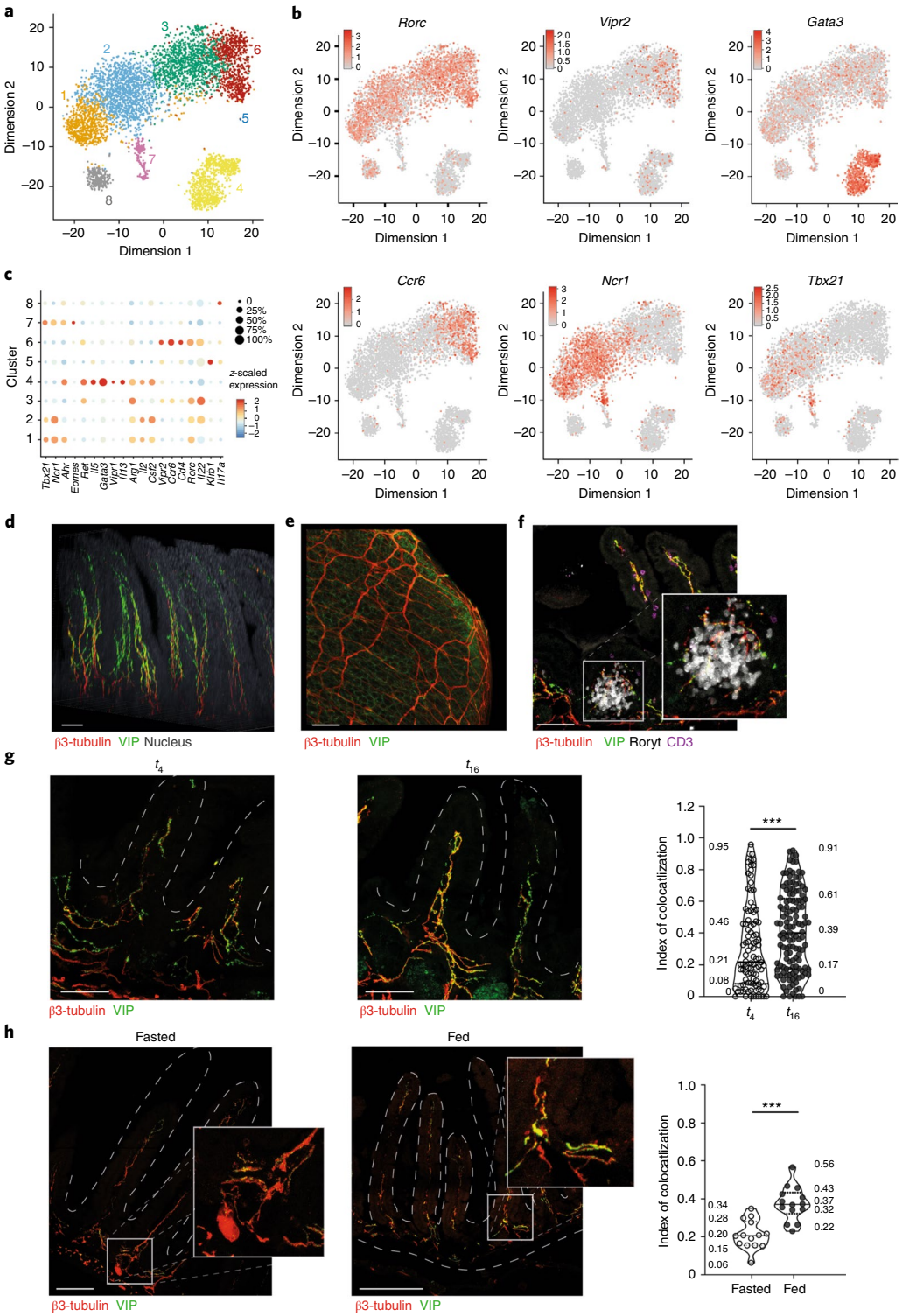

Fig. 4 | Intestinal ILC3 subsets express VIPR2 and are located close to VIP-expressing neurons. a–c, Single-cell analysis using 10× Genomics of enteric ILCs from wild-type mice. **a**, t-SNE plot showing 5,439 cells colored by cluster. **b**, $\log_2$-normalized expression of the indicated genes within the t-SNE plots. **c**, Representative differentially expressed genes (*x* axis) by cluster (*y* axis). Dot size represents the fraction of cells within the cluster that express each gene. Colors indicate the *z*-scaled expression of genes in cells within each cluster. **d**,**e**, Three-dimensional reconstruction of confocal microscopy (**d**) and light-sheet images (**e**) of a whole-mount section of small intestine stained with β3-tubulin (red), VIP (green) and cell nuclei (blue). **d**, Scale bar, 40 µm; **e**, scale bar, 200 µm. **f**, Confocal images of a frozen section of the small intestine of a *Rorc*(*γt*)$^{GFP/+}$ mouse stained for neurons (β3-tubulin; red), VIP (green), ILC3s (RORγt$^-$GFP$^+$CD3ε$^-$; white) and T cells (CD3ε$^+$; purple). Scale bar, 200 µm. **g**,**h**, Colocalization of VIP (green) in neurons (β3-tubulin; red) in enteric neuron axons from two mice per group at t_4 ($n=99$) and t_{16} ($n=133$) (**g**), or from mice fasted for 16 h or fed ad libitum (**h**). **g**, Scale bar, 50 µm; **h**, scale bar, 100 µm. Violin plots to the right show the minimum, 25th percentile, median, 75th percentile and maximum values. Statistical significance was determined by two-tailed unpaired Student's *t*-test (*$P<0.05$; **$P<0.01$; ***$P<0.001$). The results shown in **d**–**h** are representative of three (**d**) or two independent experiments (**e**–**h**). In **e**–**h**, $n=2$ mice per condition.

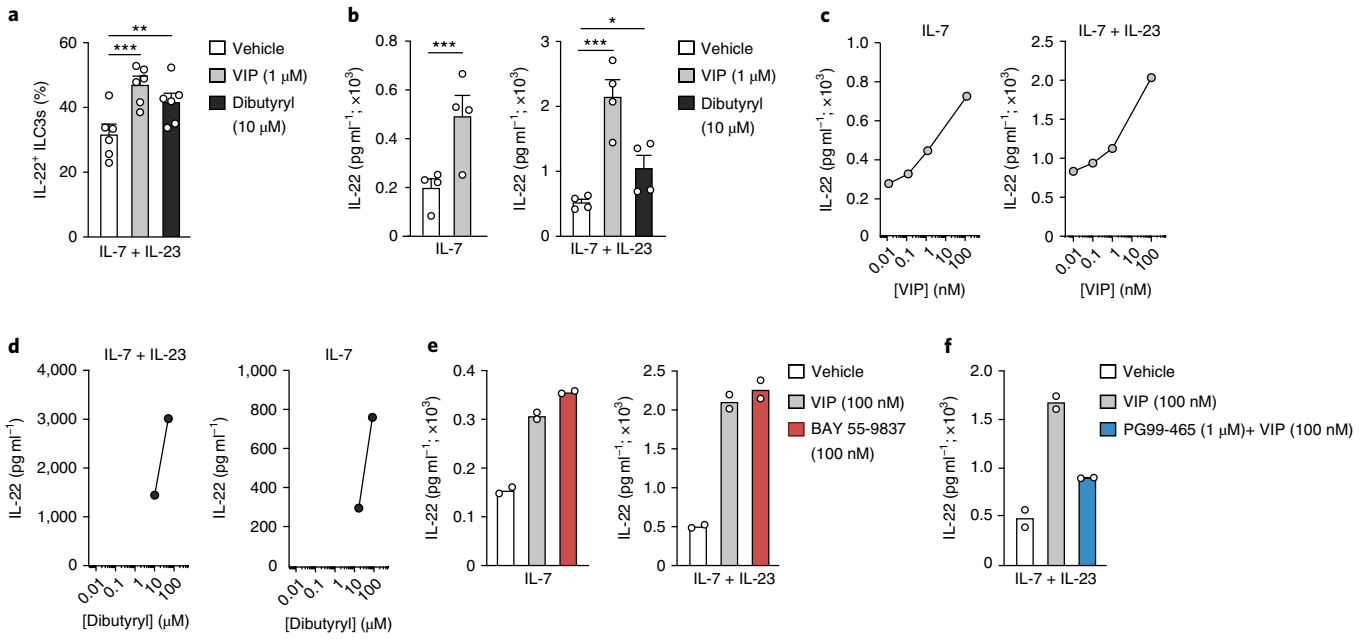

Fig. 5 | VIP directly regulates IL-22 production by ILC3s. a, Intracellular expression of IL-22 by ILC3s from mice fasted for 16 h after 4 h of incubation with IL-7 and IL-23 (10 ng ml^{-1}) in the presence of vehicle (DMSO), VIP (1 μM) or d-cAMP (dibutyryl; 10 μM). One representative experiment from four independent experiments is shown ($n = 6$ mice per experiment). **b**, IL-22 secretion by enteric ILC3s cultivated for 16 h with IL-7 ($n = 4$ biological samples) or IL-7 + IL-23 in the presence of vehicle (DMSO; $n = 4$ biological samples), VIP (1 μM; $n = 4$ biological samples) or d-cAMP ($n = 4$ biological samples). IL-22 was measured in the supernatant by ELISA. Data are pooled from three independent experiments from a total of six experiments. Data show means ± s.e.m., and statistical significance was determined by two-tailed unpaired Student's *t*-test (*$P < 0.05$; **$P < 0.01$; ***$P < 0.001$). **c**,**d**, IL-22 production by enteric ILC3s in presence of IL-7 or IL-7 + IL-23 (10 ng ml^{-1}) and the indicated concentrations of VIP (**c**) or d-cAMP (**d**). Data show means from one of three similar experiments ($n = 2$ biological samples). **e**,**f**, IL-22 production of enteric ILC3s cultured with IL-7 or IL-7 + IL-23 in the presence of VIP (100 nM; $n = 2$ biological samples) versus either the VIPR2 agonist BAY 55-9837 (100 nM; $n = 2$ biological samples) (**e**) or VIP with the VIPR2 antagonist PG99-465 (1 μM; $n = 2$ biological samples) (**f**) for 16 h. Data are pooled from two independent experiments. In **b**–**f**, each circle shows the response of enteric ILC3s pooled from two mice fed ad libitum.

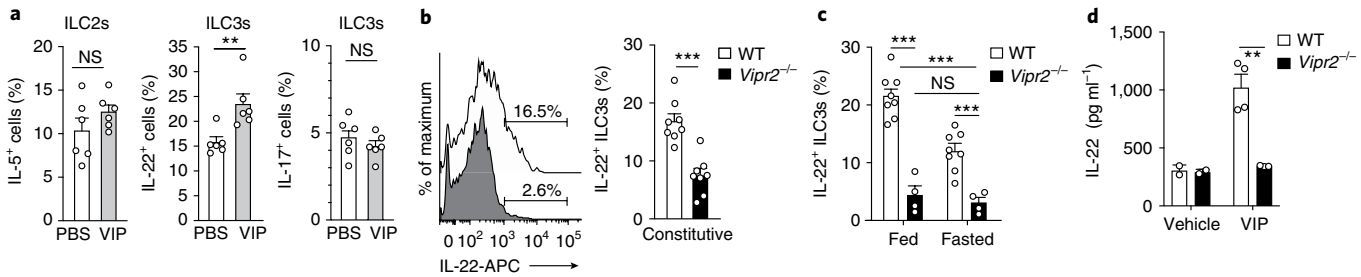

Fig. 6 | VIPR2 signaling regulates IL-22 secretion from ILC3s in vivo. a, Mice were injected intraperitoneally with 2 nM VIP or PBS 2 h (t_2) before sacrifice (t_4). Constitutive expression of IL-5 by ILC2s, and IL-22 and IL-17 by ILC3s from the small intestine, was determined by flow cytometry. Data are representative of two independent experiments ($n = 6$ mice per time point per experiment). **b**, IL-22$^+$ ILC3s isolated from the small intestine of wild-type or *Vipr2*$^{-/-}$ mice were incubated with IL-7 for 4 h. Data show means ± s.e.m. of one of two similar experiments ($n = 8$ mice per experiment). **c**, Wild-type and *Vipr2*$^{-/-}$ mice were fasted for 16 h or fed ad libitum, and the constitutive expression of IL-22 produced by ILC3s from the small intestine was determined by flow cytometry after 4 h of incubation. Data were pooled from two independent experiments ($n = 4$ wild-type mice per experiment per condition and $n = 2$ *Vipr2*$^{-/-}$ mice per experiment per condition). **d**, A total of 4.5×10^3 enteric ILC3s purified from wild-type or *Vipr2*$^{-/-}$ mice were cultivated with IL-7 and IL-23 in the presence of vehicle ($n = 2$) or VIP (1 μM; $n = 4$ for the wild-type and $n = 3$ for *Vipr2*$^{-/-}$) for 16 h. IL-22 was measured in the supernatant by ELISA. Data were pooled from two independent experiments. Each circle shows enteric ILC3s sorted from two mice. In all panels, data show means ± s.e.m., and statistical significance was determined by two-tailed unpaired Student's *t*-test (**$P < 0.01$; ***$P < 0.001$).

ILC2s and Lin$^-$Gata3$^-$Rorγt$^+$NKp46$^{+/-}$ ILC3s from the small intestine 2 h post-injection. ILC3s from VIP-injected mice had enhanced IL-22 production compared with ILC3s from PBS-injected mice (Fig. 6a), while the IL-17$^+$ ILC3s and IL-5$^+$ ILC2s were similar in VIP- and PBS-injected mice (Fig. 6a). The frequency of ILC3s that constitutively expressed IL-22 was lower in *Vipr2*$^{-/-}$ mice compared with wild-type mice (Fig. 6b). A 16-h fast reduced the expression of IL-22 in wild-type ILC3s, but had no significant impact on

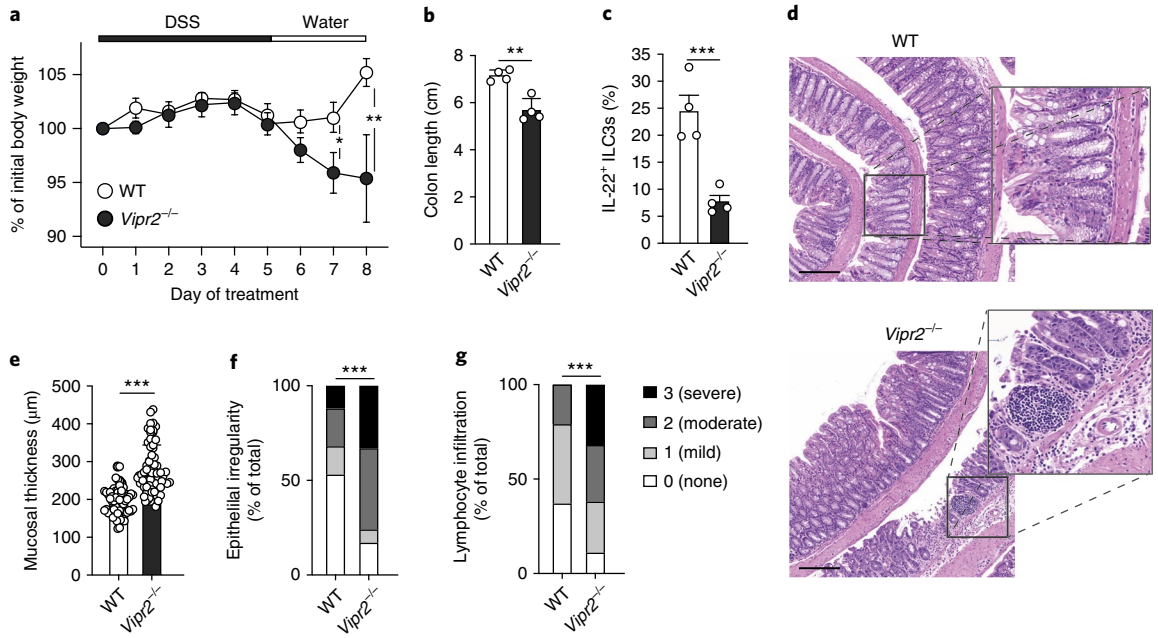

Fig. 7 | VIPR2 signaling is crucial for the regulation of gut integrity in vivo. a–g, Wild-type and *Vipr2*$^{-/-}$ mice were given water containing 1.5% DSS (wt/vol) for 5 d, followed by 3 d with regular water, and analyzed on day 8. **a**, Weights are shown as a percentage of the initial weight of wild-type and *Vipr2*$^{-/-}$ mice. **b**, Comparison of the colon lengths of wild-type and *Vipr2*$^{-/-}$ mice treated with low-dose DSS. **c**, Frequency of IL-22^{+} ILC3s isolated from the small intestine of DSS-treated mice and cultivated for 4.5 h in the presence of Brefeldin A and GolgiStop. **d**, Representative hematoxylin and eosin-stained sections of the colon from DSS-treated wild-type and *Vipr2*$^{-/-}$ mice. Scale bars: 200 μm. **e–g**, Quantitative analysis of crypt height (**e**), epithelial irregularity (**f**) and inflammatory infiltrate (**g**) in wild-type and *Vipr2*$^{-/-}$ mice. Epithelial length was measured in the distal part of the colon. Epithelial irregularity and inflammatory infiltrate were scored from six sections over two different slides per mouse (0 = normal; 1 = minor; 2 = moderate; 3 = severe). Analyses were performed across 12 randomly selected sites per mouse. In **a–c** and **e**, data show means ± s.e.m. In **a–g**, $n = 4$ mice per genotype, and one of three independent experiments is shown. In **a–c** and **e–g**, statistical significance was determined by two-tailed unpaired Student's *t*-test (*$P < 0.05$; **$P < 0.01$; ***$P < 0.001$).

the production of IL-22 in *Vipr2*$^{-/-}$ ILC3s (Fig. 6c). In contrast, constitutive expression of IL-22 in CD4^{+} T cells from the small intestine was similar in wild-type and *Vipr2*$^{-/-}$ mice (Extended Data Fig. 7b). However, the production of IL-22 in ILC3s was higher in wild-type mice fasted for 16 h than in *Vipr2*$^{-/-}$ mice (Fig. 6c), indicating that low levels of VIP in the gut, even during fasting, are sufficient to allow basal production of constitutive IL-22 by ILC3s. ILC3s purified from the small intestine of *Vipr2*$^{-/-}$ mice did not produce IL-22 when incubated with IL-7 + IL-23 in presence or absence of VIP for 16 h, in contrast with wild-type ILC3s, which strongly upregulated IL-22 under these conditions (Fig. 6d). *Vipr2*$^{-/-}$ mice had similar numbers of intestinal ILC subsets, including CD4^{+} and CD4^{-} ILC3s, compared with wild-type mice (Extended Data Fig. 7b) suggesting that VIPR2 was not required for the development or maintenance of ILC3s in the intestine. Thus, the VIP–VIPR2 axis drove the secretion of IL-22 in intestinal ILC3s in vivo.

VIPR2 in ILC3s maintains the epithelial barrier. To test whether VIP had a role in maintaining the epithelial barrier in the intestine, we treated wild-type and *Vipr2*$^{-/-}$ mice with a low dose of DSS (1.5% wt/vol) for 5 d. While wild-type mice maintained their weight until day 8 after the initiation of treatment, *Vipr2*$^{-/-}$ mice started to lose weight at day 5 (Fig. 7a) and showed more signs of severe colitis, such as shorter colon length (Fig. 7b) and a lower percentage of IL-22^{+} ILC3s (Fig. 7c). Histological analysis of the colon showed more intestinal ulceration (Fig. 7d), increased mucosal thickness (Fig. 7e), epithelial irregularity (Fig. 7f) and leukocyte infiltration (Fig. 7g) in *Vipr2*$^{-/-}$ mice compared with wild-type mice. In the absence of DSS treatment, *Vipr2*$^{-/-}$ mice did not show weight loss or epithelial damage (Extended Data Fig. 8), consistent with previous reports[40]. To determine whether the phenotype was driven by ILCs, we purified enteric Lin^{-}CD45^{+}CD127^{+}CD90^{+}CD117^{+} ILC3s from wild-type and *Vipr2*$^{-/-}$ mice and adoptively transferred them into *Rag2*$^{-/-}\gamma c^{-/-}$ recipients. Recipient mice were treated with DSS for 5 d, on days 10–14 after transfer. *Rag2*$^{-/-}\gamma c^{-/-}$ mice that received *Vipr2*$^{-/-}$ ILC3s were more susceptible to developing inflammation after DSS treatment and showed greater weight loss (Fig. 8a) and increased colon shortening (Fig. 8b), tissue disruption (Fig. 8c), mucosal thickness (Fig. 8d), epithelial irregularity (Fig. 8e) and leukocyte infiltration (Fig. 8f) compared with wild-type mice. Thus, although other intestinal lymphocytes probably contributed to the severity of the intestinal disruption in *Vipr2*$^{-/-}$ mice, VIPR2^{+} ILC3s had an important contribution in the protection of the gut epithelium during DSS-induced inflammation.

Discussion

In this study, we showed that enteric ILC3s expressed the neuropeptide receptor VIPR2 and responded to the neuropeptide VIP released by the enteric neurons. ILC3s in the gut were localized in close proximity to the enteric neurons, and VIP activated the secretion of IL-22 in ILC3s through VIPR2. VIP was strongly induced by feeding and reduced by fasting. During DSS-induced inflammation, VIPR2 expression on ILC3s contributed to the protection of the gut epithelium. Thus, neuronal VIP–VIPR2 ILC3 signaling was an important pathway dynamically controling the production of IL-22 in the gut.

The modulation of IL-22 production in ILC3s by VIP is probably part of a pathway that could prime host defenses against infection or inflammatory damage that might occur during feeding, by augmenting the so-called 'anticipatory immunity'. While transcription

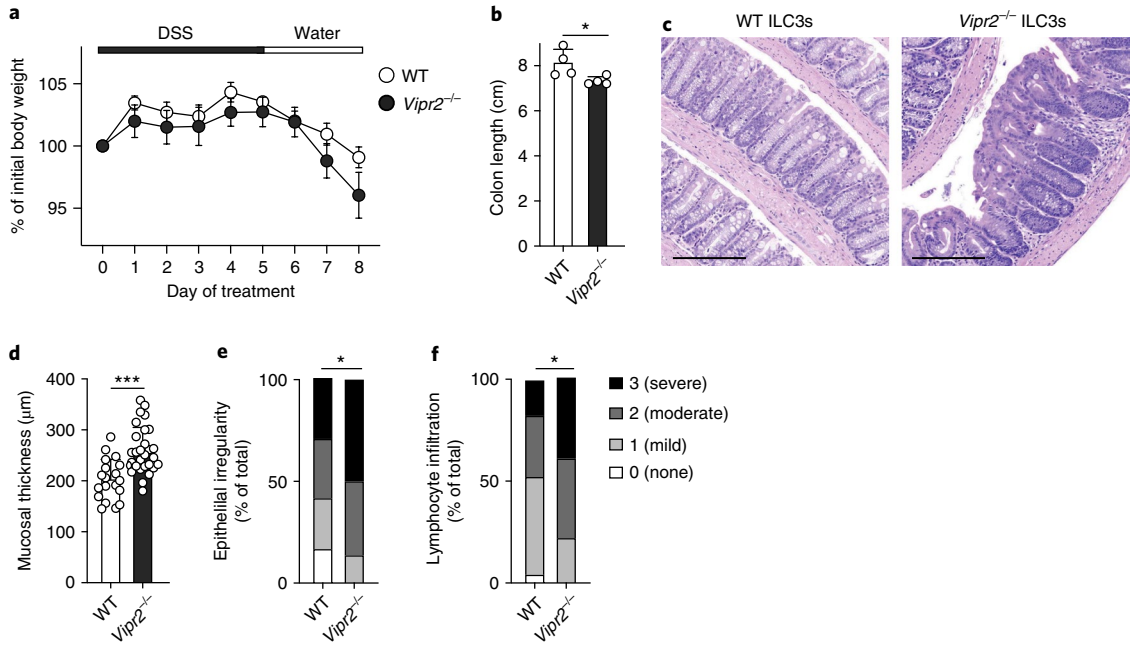

Fig. 8 | *VIPR2*$^{-/-}$ ILC3s provide protection from DSS-induced inflammation. a–f, Flow cytometrically purified ILC3s isolated from the small intestine of wild-type and *Vipr2*$^{-/-}$ mice were adoptively transferred into *Rag2*$^{-/-}\gamma c^{-/-}$ mice. After 10 d, mice were given water containing 1.5% DSS (wt/vol) for 5 d, followed by 3 d with regular water, and analyzed on day 8. **a**, Weight is shown as a percentage of the initial weight. **b**, Comparison of the colon length of DSS-treated mice reconstituted with wild-type or *Vipr2*$^{-/-}$ ILC3s. **c**, Representative hematoxylin and eosin-stained sections of tissues from DSS-treated mice. Scale bars: 200 μm. **d–f**, Quantitative analysis of crypt height (**d**), epithelial irregularity (**e**) and inflammatory infiltrate (**f**) in DSS-treated mice reconstituted with wild-type or *Vipr2*$^{-/-}$ ILC3s. Epithelial length was measured in the distal part of the colon. Epithelial irregularity and inflammatory infiltrate was scored from six sections over two different slides per mouse (0 = normal; 1 = minor; 2 = moderate; 3 = severe). Analyses were performed across 12 randomly selected sites per mouse. In **a**, **b** and **d**, data show means ± s.e.m. In **a–f**, $n = 4$ mice per genotype, and one of three independent experiments is shown. In **b** and **d–f**, statistical significance was determined by two-tailed unpaired Student's *t*-test (*$P < 0.05$; **$P < 0.01$; ***$P < 0.001$).

factors associated with the circadian clock machinery intrinsically imprint a 12-h cycle in innate cells, we showed that local cues, such as feeding-induced production of VIP, acted independent of the circadian clock regulatory programs.

It has been reported that neuroimmune hubs composed of various lymphocyte subsets, metabolic mediators and neuronal regulators play a key role in orchestrating context-dependent immune protection[8,23,26,41–43]. We found that intestinal ILC3s were regulated by intrinsic signals from the circadian clock regulator ARNTL, as well as extrinsic feeding signals, which were also cyclically regulated. Loss of ARNTL was previously reported to lead to a decrease of IL-22-producing ILC3s[32], consistent with our findings. However, changes in the feeding regimen only partially altered the expression of circadian genes in ILC3s[32], suggesting that the food-dependent modulation of IL-22 production in ILC3s we report here might be independent of the ARNTL-controlled circadian rythms, and that a combination of intrinsic and extrinsic factors could be responsible for the modulation of ILC3 circadian activity. Uncoupling of the intrinsic and extrinsic regulation of ILC3 activation through the genetic ablation of ARNTL showed that production of IL-22 in ILC3s correlated with feeding patterns, which could potentially influence cellular metabolism and signaling in ILC3s. ILCs are thought to be almost exclusively lodged within tissues and positioned at barrier surfaces, with little migratory capacity or ability to exert influence beyond the tissue of residence[44,45]. How distinct subsets of ILCs protect the various mucosal barriers in the body remains unclear. ILC2s can be mobilized from the bone marrow and can traffic to the lung during helminth infection through IL-25-dependent regulation of expression of the sphingosine 1-phosphate receptor on ILC2—a process regulated by the lipid mediator sphingosine 1-phosphate[46] and ARNTL[47]. The VIP–VIPR2 signaling regulates ILC2 release of IL-5 and drives the accumulation of lymphocytes in the lung[23]. Eosinophil recruitment and accumulation in the lung were linked with postprandial induction of IL-5 in intestinal ILC2s[23]. We found that production of IL-5 by intestinal ILC2s was not intrinsically regulated by ARNTL, suggesting that multiple distinct mechanisms regulate ILC2 function, allowing both local and distant immune regulatory effects. We found that production of IL-22 in ILC3s was tissue specific and was modulated by direct exposure to VIP from enteric neurons. Deletion of VIPR2 indicated a requirement for VIP–VIPR2 signaling in controlling intestinal inflammation during DSS exposure. This is consistent with the protective role of IL-22 during inflammatory bowel disease and chronic colitis in humans[48,49] and mouse models[7,50]. Thus, our observations identify one of the signals that modulate the expression of IL-22 in the intestine, and are probably important in the immunopathology associated with IL-22 as well. These observations reveal some of the mechanisms that match the protective responses in the intestine with the stimulatory burden in the gut and possibly orchestrate the induction of homeostatic tissue repair pathways.

Online content

Any methods, additional references, Nature Research reporting summaries, source data, extended data, supplementary information, acknowledgements, peer review information; details of author contributions and competing interests; and statements of data and code availability are available at https://doi.org/10.1038/s41590-019-0567-y.

Received: 11 June 2019; Accepted: 22 November 2019;
Published online: 23 December 2019

References

1. Sender, R., Fuchs, S. & Milo, R. Are we really vastly outnumbered? Revisiting the ratio of bacterial to host cells in humans. *Cell* **164**, 337–340 (2016).
2. Scheiermann, C., Kunisaki, Y. & Frenette, P. S. Circadian control of the immune system. *Nat. Rev. Immunol.* **13**, 190–198 (2013).
3. Sonnenberg, G. F. et al. Innate lymphoid cells promote anatomical containment of lymphoid-resident commensal bacteria. *Science* **336**, 1321–1325 (2012).
4. Rankin, L. C. et al. Complementarity and redundancy of IL-22-producing innate lymphoid cells. *Nat. Immunol.* **17**, 179–186 (2016).
5. Mortha, A. et al. Microbiota-dependent crosstalk between macrophages and ILC3 promotes intestinal homeostasis. *Science* **343**, 1249288 (2014).
6. Lindemans, C. A. et al. Interleukin-22 promotes intestinal-stem-cell-mediated epithelial regeneration. *Nature* **528**, 560–564 (2015).
7. Zenewicz, L. A. et al. Innate and adaptive interleukin-22 protects mice from inflammatory bowel disease. *Immunity* **29**, 947–957 (2008).
8. Ibiza, S. et al. Glial-cell-derived neuroregulators control type 3 innate lymphoid cells and gut defence. *Nature* **535**, 440–443 (2016).
9. Hasegawa, M. et al. Interleukin-22 regulates the complement system to promote resistance against pathobionts after pathogen-induced intestinal damage. *Immunity* **41**, 620–632 (2014).
10. Zheng, Y. et al. Interleukin-22 mediates early host defense against attaching and effacing bacterial pathogens. *Nat. Med.* **14**, 282–289 (2008).
11. Lee, J. S. et al. AHR drives the development of gut ILC22 cells and postnatal lymphoid tissues via pathways dependent on and independent of Notch. *Nat. Immunol.* **13**, 144–151 (2011).
12. Sonnenberg, G. F., Monticelli, L. A., Elloso, M. M., Fouser, L. A. & Artis, D. $CD4^+$ lymphoid tissue-inducer cells promote innate immunity in the gut. *Immunity* **34**, 122–134 (2011).
13. Zelante, T. et al. Tryptophan catabolites from microbiota engage aryl hydrocarbon receptor and balance mucosal reactivity via interleukin-22. *Immunity* **39**, 372–385 (2013).
14. Lamas, B. et al. CARD9 impacts colitis by altering gut microbiota metabolism of tryptophan into aryl hydrocarbon receptor ligands. *Nat. Med.* **22**, 598–605 (2016).
15. Wang, Y., Mumm, J. B., Herbst, R., Kolbeck, R. & Wang, Y. IL-22 increases permeability of intestinal epithelial tight junctions by enhancing claudin-2 expression. *J. Immunol.* **199**, 3316–3325 (2017).
16. Peters, C. P., Mjosberg, J. M., Bernink, J. H. & Spits, H. Innate lymphoid cells in inflammatory bowel diseases. *Immunol. Lett.* **172**, 124–131 (2016).
17. Kirchberger, S. et al. Innate lymphoid cells sustain colon cancer through production of interleukin-22 in a mouse model. *J. Exp. Med.* **210**, 917–931 (2013).
18. Huber, S. et al. IL-22BP is regulated by the inflammasome and modulates tumorigenesis in the intestine. *Nature* **491**, 259–263 (2012).
19. Gury-BenAri, M. et al. The spectrum and regulatory landscape of intestinal innate lymphoid cells are shaped by the microbiome. *Cell* **166**, 1231–1246.e13 (2016).
20. Colonna, M. Innate lymphoid cells: diversity, plasticity, and unique functions in immunity. *Immunity* **48**, 1104–1117 (2018).
21. Laffont, S. et al. Androgen signaling negatively controls group 2 innate lymphoid cells. *J. Exp. Med.* **214**, 1581–1592 (2017).
22. Quatrini, L. et al. Host resistance to endotoxic shock requires the neuroendocrine regulation of group 1 innate lymphoid cells. *J. Exp. Med.* **214**, 3531–3541 (2017).
23. Nussbaum, J. C. et al. Type 2 innate lymphoid cells control eosinophil homeostasis. *Nature* **502**, 245–248 (2013).
24. Wallrapp, A. et al. The neuropeptide NMU amplifies ILC2-driven allergic lung inflammation. *Nature* **549**, 351–356 (2017).
25. Klose, C. S. N. et al. The neuropeptide neuromedin U stimulates innate lymphoid cells and type 2 inflammation. *Nature* **549**, 282–286 (2017).
26. Cardoso, V. et al. Neuronal regulation of type 2 innate lymphoid cells via neuromedin U. *Nature* **549**, 277–281 (2017).
27. Barrow, A. D. & Colonna, M. Innate lymphoid cell sensing of tissue vitality. *Curr. Opin. Immunol.* **56**, 82–93 (2018).
28. Rankin, L. C. et al. The transcription factor T-bet is essential for the development of $NKp46^+$ innate lymphocytes via the Notch pathway. *Nat. Immunol.* **14**, 389–395 (2013).
29. Mukherji, A., Kobiita, A., Ye, T. & Chambon, P. Homeostasis in intestinal epithelium is orchestrated by the circadian clock and microbiota cues transduced by TLRs. *Cell* **153**, 812–827 (2013).
30. Yu, X. et al. T_H17 cell differentiation is regulated by the circadian clock. *Science* **342**, 727–730 (2013).
31. Curtis, A. M., Bellet, M. M., Sassone-Corsi, P. & O'Neill, L. A. Circadian clock proteins and immunity. *Immunity* **40**, 178–186 (2014).
32. Godinho-Silva, C. et al. Light-entrained and brain-tuned circadian circuits regulate ILC3s and gut homeostasis. *Nature* **574**, 254–258 (2019).
33. Acosta-Rodriguez, V. A., de Groot, M. H. M., Rijo-Ferreira, F., Green, C. B. & Takahashi, J. S. Mice under caloric restriction self-impose a temporal restriction of food intake as revealed by an automated feeder system. *Cell Metab.* **26**, 267–277.e2 (2017).
34. van der Maaten, L. & Hinton, G. Visualizing data using t-SNE. *J. Mach. Learn. Res.* **9**, 2579–2605 (2008).
35. Watanabe, K., Vanecek, J. & Yamaoka, S. In vitro entrainment of the circadian rhythm of vasopressin-releasing cells in suprachiasmatic nucleus by vasoactive intestinal polypeptide. *Brain Res.* **877**, 361–366 (2000).
36. Colwell, C. S. et al. Disrupted circadian rhythms in VIP- and PHI-deficient mice. *Am. J. Physiol. Regul. Integr. Comp. Physiol* **285**, R939–R949 (2003).
37. Harmar, A. J. et al. The $VPAC_2$ receptor is essential for circadian function in the mouse suprachiasmatic nuclei. *Cell* **109**, 497–508 (2002).
38. Lelievre, V. et al. Gastrointestinal dysfunction in mice with a targeted mutation in the gene encoding vasoactive intestinal polypeptide: a model for the study of intestinal ileus and Hirschsprung's disease. *Peptides* **28**, 1688–1699 (2007).
39. Schwede, F., Maronde, E., Genieser, H. & Jastorff, B. Cyclic nucleotide analogs as biochemical tools and prospective drugs. *Pharmacol. Ther.* **87**, 199–226 (2000).
40. Yadav, M., Huang, M. C. & Goetzl, E. J. VPAC1 (vasoactive intestinal peptide (VIP) receptor type 1) G protein-coupled receptor mediation of VIP enhancement of murine experimental colitis. *Cell Immunol.* **267**, 124–132 (2011).
41. Veiga-Fernandes, H. & Mucida, D. Neuro-immune interactions at barrier surfaces. *Cell* **165**, 801–811 (2016).
42. Veiga-Fernandes, H. & Pachnis, V. Neuroimmune regulation during intestinal development and homeostasis. *Nat. Immunol.* **18**, 116–122 (2017).
43. Moriyama, S. et al. β2-adrenergic receptor-mediated negative regulation of group 2 innate lymphoid cell responses. *Science* **359**, 1056–1061 (2018).
44. Gasteiger, G., Fan, X., Dikiy, S., Lee, S. Y. & Rudensky, A. Y. Tissue residency of innate lymphoid cells in lymphoid and nonlymphoid organs. *Science* **350**, 981–985 (2015).
45. Fan, X. & Rudensky, A. Y. Hallmarks of tissue-resident lymphocytes. *Cell* **164**, 1198–1211 (2016).
46. Huang, Y. et al. S1P-dependent interorgan trafficking of group 2 innate lymphoid cells supports host defense. *Science* **359**, 114–119 (2018).
47. Druzd, D. et al. Lymphocyte circadian clocks control lymph node trafficking and adaptive immune responses. *Immunity* **46**, 120–132 (2017).
48. Cella, M. et al. A human natural killer cell subset provides an innate source of IL-22 for mucosal immunity. *Nature* **457**, 722–725 (2009).
49. Andoh, A., Bamba, S., Fujiyama, Y., Brittan, M. & Wright, N. A. Colonic subepithelial myofibroblasts in mucosal inflammation and repair: contribution of bone marrow-derived stem cells to the gut regenerative response. *J. Gastroenterol.* **40**, 1089–1099 (2005).
50. Sanos, S. L. et al. RORγt and commensal microflora are required for the differentiation of mucosal interleukin 22-producing $NKp46^+$ cells. *Nat. Immunol.* **10**, 83–91 (2009).

Publisher's note Springer Nature remains neutral with regard to jurisdictional claims in published maps and institutional affiliations.

© The Author(s), under exclusive licence to Springer Nature America, Inc. 2019

Methods

Mice. *Arntl*$^{fl/fl}$ (B6.129S4(Cg)-*Arntl*^{tm1Weit}/J)[51], *Il7r*^{Cre} (ref. [52]), *Vipr2*$^{-/-}$ (B6.129P2-*Vipr2*^{tm1Ajh}/J) (ref. [53]), *Rorc(γt)*$^{+/GFP}$ (ref. [54]) and *Rag2*$^{-/-}\gamma c^{-/-}$ (ref. [55]) mice were maintained on a C57BL/6 (Ly5.2) background (all originally derived from The Jackson Laboratory) and have been described previously. *Arntl*$^{fl/fl}$ mice were crossed to the *Il7r*^{Cre} strain to generate the *Arntl*$^{fl/fl}$*Il7r*^{Cre} line that lacks ARNTL in all lymphocytes. C57BL/6, B6.SJL-*Ptprc*^{a}*Pep3*^{b}/BoyJ (Ly5.1$^{+/+}$; CD45.1$^{+/+}$) and CD45.1^{+}CD45.2^{+}(F1) mice were bred and maintained in-house. Mice were housed under a 12 h/12 h light–dark cycle under controlled-temperature conditions with food and water ad libitum unless otherwise indicated. For time-restricted feeding experiments, food was removed for a period of 12 h either during the day or during the night, with water available ad libitum. For some experiments, mice were fasted overnight for a period of 16 h. When not stipulated, mice were analyzed at t_4 after the onset of light, and food access was not restricted. Mice were bred and maintained in specific pathogen-free conditions at the Walter and Eliza Hall Institute of Medical Research. All mice were used at 7–12 weeks of age. Animals were handled according to the guidelines of the Australian Code for the Care and Use of Animals of the National Health and Medical Research Council of Australia. Experimental procedures were approved by the Animal Ethics Committee of the Walter and Eliza Hall Institute of Medical Research.

Isolation of lymphoid cells. Single-cell suspensions of lymphocytes were isolated from the small intestine and colon following incubation for 40 min at 37 °C in Ca^{2+}- and Mg^{2+}-free Hanks media containing 2% fetal calf serum (FCS) and 1 mM EDTA, with gentle shaking to remove intestinal epithelial cells[4,28]. The supernatant was discarded and tissues were then incubated, with gentle shaking, with 1 mg ml^{-1} (wt/vol) Collagenase IV (Worthington), 200 μg ml^{-1} DNase I (Roche) and 4 U ml^{-1} Dispase (Sigma–Aldrich) in RPMI-1640 + 2% (vol/vol) heat-inactivated FCS for 45 min at 37 °C. Lungs were cut into small fragments and digested for 45 min at 37 °C with 1 mg ml^{-1} Collagenase IV and 200 μg ml^{-1} DNase I. Preparations were filtered and mononuclear cells were isolated by centrifugation on a 40–80% Percoll gradient. Lymphocytes were recovered from the interface and washed twice. Single-cell suspensions were generated from the mesenteric lymph node by gently dissociating tissues using 70-μm filters. Cells were resuspended in PBS supplemented with 1 mM EDTA.

Flow cytometry. Single-cell suspensions were stained with the following antibodies: TCRβ (H57-597) from BioLegend; CD19 (ID3), CD3ε (145-2C11), ICOS (C398.4A), NKp46 (29A1.4), NK1.1 (PK136), CD117 (2B8), CD127 (IL-7R, A7R34), Sca-1 (D7) and ST2 (RMST2-2) from eBioscience; and CD11b (M1/70), KLRG1 (2F1), CD45R/B220 (RA3-6B2), CD45.1 (A20) CD45.2 (104), CD90.2 (30-H12) and CD49a (Ha31/8) from BD Biosciences. Intracellular staining was performed using the Transcription Factor Staining Buffer Set (eBioscience) and antibodies against GATA-3 (TWAJ), Rorγt (AFKJS-9; BD Biosciences) and EOMES (Dan11mag; eBioscience) and cytokines IL-5 (TRFK5; eBioscience), IL-13 (eBio13A; eBioscience), IL-17A (eBio17B7; eBioscience) and IL-22 (IL22JOP; eBioscience). Cells were analyzed using a FACSCanto II or Fortessa X20 (BD Biosciences) and FlowJo software was used for analysis. Flow cytometric sorting was performed with a FACSAria III (BD Biosciences).

ILC3 isolation and in vitro stimulation. Cells isolated by digestion from the small intestinal tissue were stained for 30 min with optimally titered antibodies against CD90.2, NKp46, NK1.1, CD117, IL-7Rα, KLRG1, B220, CD19, CD3, CD11b and CD45. ILC3s were identified as CD45^{+}CD90^{+}CD117^{+}IL-7Rα^{+}NKp46$^{+/-}$ and negative for KLRG1, B220, CD19, CD3, CD11b and NK1.1. Stained cells were washed and sorted using a FACSAria III (BD Biosciences). Purified cells were cultivated in complete RPMI-1640 containing 10% heat-inactivated FCS, 1 mM L-glutamine, 100 U ml^{-1} penicillin, 100 μg ml^{-1} streptomycin and 50 μM β-mercaptoethanol. The cytokine expression of ILCs was determined as follows: cells were stimulated for 4.5 h in the presence of 1 ng ml^{-1} PMA, 1 μg ml^{-1} ionomycin and 10 μg ml^{-1} Brefeldin A and GolgiStop (BD Biosciences). To test the constitutive secretion of cytokines, ILCs were incubated for 4.5 h in the presence of 10 μg ml^{-1} Brefeldin A. For longer-term cultures, media was supplemented with 10 ng ml^{-1} recombinant human IL-7 (R&D Systems) (a survival factor), with or without 10 ng ml^{-1} recombinant murine IL-23 (R&D Systems). To test the effect of VIP on ILC3s, cells were incubated with different concentrations of VIP (human, rat, mouse, rabbit, canine or porcine) from Tocris, BA55-9837 (Tocris), PG99-465 (Myristoyl-(Lys12·27·28)-VIP-Gly-Gly-Thr (free acid) trifluoroacetate salt; Bachem) or d-cAMP (Tocris). All reagents were resuspended in sterile water, except d-cAMP, which was resuspended in dimethyl sulfoxide (DMSO). To measure IL-22, purified ILC3s were cultured for 16 h under the above conditions and the supernatant was analyzed using the IL-22 ELISA Kit (Thermo Fisher Scientific), following the manufacturer's recommendations.

In vivo activation with exogenous VIP. For all in vivo experiments with VIP treatment, an intraperitoneally administered dose of 2 nmol VIP in PBS per mouse or PBS alone was injected 2 h before tissue harvest.

DSS-induced colitis. DSS (molecular mass: 36,000–50,000 Da; MP Biomedicals) was added to drinking water 1.5% (wt/vol) for 5 d, followed by 3 d of regular water. Mice were analyzed on day 8. Mice were monitored daily for weight loss, stool consistency and hematochezia. In some experiments, 1.5–1.7 × 10^{4} flow cytometrically purified *Vipr2*$^{-/-}$ or wild-type ILC3s were adoptively transferred into *Rag2*$^{-/-}\gamma c^{-/-}$ recipient mice and allowed to reconstitute for 10 d. Mice were then subjected to DSS treatment for 5 d, followed by 3 d with regular water before analysis on day 8.

RNA–Seq and analyses. ILC2s and ILC3s were purified by flow cytometric sorting (FACSAria III; BD Biosciences) at four different time points (t_4, t_{10}, t_{16} and t_{23}) from female wild-type mice. One to two biological replicates were generated for each subset from the small intestine. RNA was isolated using a QIAGEN RNeasy Micro kit. Libraries were generated using the Illumina TruSeq RNA sample preparation kit, following the manufacturer's instructions, and subjected to transcriptome 85-base pair single-end sequencing on an Illumina NextSeq instrument. Reads were aligned to the GRCm38/mm10 build of the *Mus musculus* genome using the Rsubread aligner[56,57]. Uniquely mapped reads were retained and genewise counts were obtained using featureCounts[56] and RefSeq (National Center for Biotechnology Information) annotation. Differential expression analyses were then undertaken using the edgeR[58] and limma[59] software packages. Lowly expressed genes were filtering using edgeR's filterByExpr function with default settings. Additionally, genes without current annotation, ribosomal RNAs, nonprotein-coding immunoglobulins, predicted/unknown/pseudo genes and those not on known chromosomes were also removed. Compositional differences between libraries were normalized using the trimmed mean of log-expression ratios (TMM) method[60]. To remove unwanted variation from the data and adjust for differences between the ILC2 and ILC3 samples, the RUVIII algorithm from the ruv software package[61] was applied with $k = 4$ to the $\log_2$[counts per million]-transformed data. A single harmonic sinusoidal model was then fit to the corrected data and cyclic genes were identified using robust empirical Bayes-moderated *t*-statistics with a trended prior variance[62]. *P* values were adjusted using the Benjamini and Hochberg method to control the false discovery rate below 5%. Analysis of the Reactome database was carried out using limma's kegga function. The heatmap was generated using the CRAN package pheatmap (version 1.0.12).

Single-cell RNA–Seq and analysis. For single-cell RNA–Seq, ILCs were sorted as li n^{-}(CD3ε^{-}TCRβ^{-}CD19^{-}B220^{-}Gr1^{-}CD11b^{-})CD45^{+}IL-7R^{+}CD90^{+} cells into ice-cold 0.5% bovine serum albumin (BSA) in PBS and processed through the Chromium Single Cell 3′ v2 Library Kit (10× Genomics), according to the manufacturer's protocol. Each channel was loaded with 20,000 cells from each tissue, yielding 5,439–7,388 single cells for analysis from the small intestine and colon. The cells were then partitioned into gel beads in emulsion in the instrument, where cell lysis and barcoded reverse transcription of RNA occurred, followed by amplification, shearing, and 5′-adapter and sample index attachment. Libraries were sequenced on an Illumina NextSeq platform. Reads from each sample were processed separately using 10× Genomics Cell Ranger software (version 3.0.2). Cellranger mkfastq was used to demultiplex the Illumina sequencer's base for each flowcell directory into FASTQ files. Next, 'cellranger count' was used to generate single-cell gene-count matrices against the 10× Genomics pre-built mm10 reference genome and transcriptome (version 3.0.0). All subsequent analysis was performed in R (version 3.6.0)[63], Bioconductor (version 3.9)[64] and simpleSingleCell workflow[65]. The DropletUtils package (version 1.4.0) was used to create a SingleCellExperiment for each sample from the Cell Ranger output directories and to identify empty droplets[66]. Quality control on the cells was performed using the scater package (version 1.12.2)[67] with two rounds of outlier detection and removal. Cells were declared as outliers and removed if they satisfied any of the following criteria: (1) read counts more than three median absolute deviations (MADs) below the median ($\log_{10}$ scale); (2) gene numbers detected more than three MADs below the median ($\log_{10}$ scale); and (3) percentages of reads coming from the mitochondria more than three MADs above the median. Detection of doublet libraries was performed using a two-stage strategy similar to that reported by Pijuan-Sala et al.[68]. In total, this identified 262 putative doublets (211 from the fed colon and 51 from the fed small intestine), which were removed from subsequent analysis. We then performed principal component analysis across all samples and, using the mutual nearest neighbor-corrected values, we applied t-SNE using the Rtsne package (version 0.13) (https://cran.r-project.org/web/packages/Rtsne). To identify cluster-specific marker genes, we performed Welch's *t*-tests on the log-expression values for every gene and between every pair of clusters.

Histology and confocal imaging. For histological analyses, tissues were fixed in 10% neutral buffered formalin and processed for wax embedding and routine hematoxylin and eosin staining. Tissues were analyzed with Aperio ImageScope (version 11.2.0.780) software, and features were blindly scored for the presence of mucosal ulceration, mucosal height, epithelial irregularity and lymphocyte infiltration using the following grading system: 0 = no changes; 1 = mild changes; 2 = moderate changes; and 3 = severe changes.

For confocal imaging analysis, intestinal tissues were gently flushed with PBS, then cut longitudinally and formed into a 'Swiss roll' for visualization of the full length of the tissue. After fixation of 4% paraformaldehyde for 2 h, the Swiss rolls were dehydrated overnight in 30% sucrose before being embedded in OCT, frozen

and stored at −80 °C. Frozen tissues were sliced using a cryostat to 20-µm-thick sections and fixed in cold acetone for 10 min. Tissues were washed with PBS, then blocked with PBS containing 3% BSA and 0.3% Triton X-100 for 2 h at room temperature. Tissue sections were then rinsed in staining buffer (1% BSA and 0.3% Triton X-100 in PBS) and incubated with anti-GFP Alexa Fluor 488 (Thermo Fisher Scientific), anti-β3-tubulin Alexa 594 (TUBB3; BioLegend) or anti-VIP Alexa 647 (H-6; Santa-Cruz), plus anti-CD3ε Pacific Blue (OKT3; eBioscience), Hoechst 33342 (Thermo Fisher Scientific) or SYTO 24 (Invitrogen). Tissues were stained overnight at 4 °C with antibodies diluted in PBS containing 1% BSA and 0.3% Triton X-100 (Sigma–Aldrich). Tissue sections were then washed three times then mounted with ProLong Gold mounting medium (Invitrogen). Images were acquired on a Zeiss LSM 880 NLO confocal microscope.

For whole-mount staining, small intestinal tissues were cleaned and cut into small sections (~0.5 cm). Sections were fixed in 4% paraformaldehyde for 2 h at room temperature. Afterwards, the tissue was washed in PBS and blocked with PBS containing 3% BSA and 0.3% Triton X-100 for 12 h. The tissue was stained for 48 h at 4 °C with the following antibodies: anti-β3-tubulin Alexa 594, anti-VIP Alexa 647 and anti-CD3ε Pacific Blue or Hoechst 33342. Subsequently gut samples were cleared using Ce3D reagent[69]. The tissue was then embedded in low-melting-temperature agarose (Bio-Rad) in a 1-ml syringe, to be imaged with a Zeiss Z.1 light-sheet microscope, or mounted on a microscope slide and captured under a Zeiss LSM 880 NLO confocal microscope equipped with Zen software (Zeiss). Surface reconstruction was performed using Imaris software (version 9.3; Bitplane). Data analyses were performed via a custom macro in FIJI[70].

To determine the colocalization of VIP-expressing neurons and ILC3s, we used a custom-written ImageJ macro. Initially we created a mask to define the axons of the neurons, to allow us to define their localization and then compare the staining area of VIP and β3-tubulin. Within each of these areas, we filtered to reduce noise and thresholded. These thresholded images were then filtered for signals greater than 5 pixels in each channel in the selected area, to determine the positive area of each signal. The area positive for VIP signal (referred to as $area_{VIP}$) and the area positive for β3-tubulin (referred to as $area_{β3\text{-}tubulin}$) was generated. To determine the area of overlap between the signals for these two molecules, the intersection of the two areas was calculated as: $[area_{VIP} \cap area_{β3\text{-}tubulin}]$. To determine colocalization between the pixels positive for VIP and β3-tubulin, independent of the size of surface analyzed, we calculated the index as: $[area_{VIP} \cap area_{β3\text{-}tubulin}]/area_{β3\text{-}tubulin}$.

Oral antibiotic treatment. Mice were given unrestricted access to drinking water containing a mix of ampicillin (1 mg ml^{-1}), streptomycin (5 mg ml^{-1}) and colistin (1 mg ml^{-1}) (Sigma–Aldrich) for 2 weeks[71–73]. Gut decontamination was evaluated by macroscopic evaluation of cecal hypertrophy.

Statistical analysis. All statistical analyses were performed with GraphPad Prism software (version 7.0 or 8.0; Graphpad Software). An unpaired two-tailed Student's *t*-test was used for pairwise comparisons. An unpaired or paired Student's *t*-test, nonparametric Mann–Whitney *U*-test or log-rank Mantel–Cox test was used for the other comparisons. All experiments were performed at least twice, with similar results obtained each time. For visualization of the circadian patterns, we performed cosinor fitting of circadian curves using the curve-fitting module of GraphPad Prism, with the equation: $Y = \text{baseline} + \text{amplitude} \times cos(\text{frequency}\ X + \text{phaseshift})$, where baseline is the average of Y_{max} and Y_{min}, $\text{amplitude} = 0.5 \times (Y_{max} - Y_{min})$, $\text{frequency} = 0.2618\ (2\pi/24)$ and phaseshift is the value of X at Y_{max}.

Reporting Summary. Further information on research design is available in the Nature Research Reporting Summary linked to this article.

Data availability

Single-cell RNA–Seq profiling data that support the findings of this study have been deposited in the Gene Expression Omnibus repository with the accession code GSE132273.

References

51. Storch, K. F. et al. Intrinsic circadian clock of the mammalian retina: importance for retinal processing of visual information. *Cell* **130**, 730–741 (2007).
52. Schlenner, S. M. et al. Fate mapping reveals separate origins of T cells and myeloid lineages in the thymus. *Immunity* **32**, 426–436 (2010).
53. Goetzl, E. J. et al. Enhanced delayed-type hypersensitivity and diminished immediate-type hypersensitivity in mice lacking the inducible $VPAC_2$ receptor for vasoactive intestinal peptide. *Proc. Natl Acad. Sci. USA* **98**, 13854–13859 (2001).
54. Eberl, G. et al. An essential function for the nuclear receptor RORγt in the generation of fetal lymphoid tissue inducer cells. *Nat. Immunol.* **5**, 64–73 (2004).
55. Garcia, S., DiSanto, J. & Stockinger, B. Following the development of a CD4 T cell response in vivo: from activation to memory formation. *Immunity* **11**, 163–171 (1999).
56. Liao, Y., Smyth, G. K. & Shi, W. featureCounts: an efficient general purpose program for assigning sequence reads to genomic features. *Bioinformatics* **30**, 923–930 (2014).
57. Liao, Y., Smyth, G. K. & Shi, W. The Subread aligner: fast, accurate and scalable read mapping by seed-and-vote. *Nucleic Acids Res.* **41**, e108 (2013).
58. Robinson, M. D., McCarthy, D. J. & Smyth, G. K. edgeR: a Bioconductor package for differential expression analysis of digital gene expression data. *Bioinformatics* **26**, 139–140 (2010).
59. Ritchie, M. E. et al. *limma* powers differential expression analyses for RNA-sequencing and microarray studies. *Nucleic Acids Res.* **43**, e47 (2015).
60. Robinson, M. D. & Oshlack, A. A scaling normalization method for differential expression analysis of RNA-Seq data. *Genome Biol.* **11**, R25 (2010).
61. Gagnon-Bartsch, J. A. & Speed, T. P. Using control genes to correct for unwanted variation in microarray data. *Biostatistics* **13**, 539–552 (2012).
62. Phipson, B., Lee, S., Majewski, I. J., Alexander, W. S. & Smyth, G. K. Robust hyperparameter estimation protects against hypervariable genes and improves power to detect differential expression. *Ann. Appl. Stat.* **10**, 946–963 (2016).
63. R Development Core Team. *R: A Language and Environment for Statistical Computing* (R Foundation for Statistical Computing, 2018).
64. Huber, W. et al. Orchestrating high-throughput genomic analysis with bioconductor. *Nat. Methods* **12**, 115–121 (2015).
65. Lun, A. T., McCarthy, D. J. & Marioni, J. C. A step-by-step workflow for low-level analysis of single-cell RNA-Seq data with Bioconductor. *F1000Res* **5**, 2122 (2016).
66. Lun, A. T. L. et al. EmptyDrops: distinguishing cells from empty droplets in droplet-based single-cell RNA sequencing data. *Genome Biol.* **20**, 63 (2019).
67. McCarthy, D. J., Campbell, K. R., Lun, A. T. & Wills, Q. F. Scater: pre-processing, quality control, normalization and visualization of single-cell RNA-Seq data in R. *Bioinformatics* **33**, 1179–1186 (2017).
68. Pijuan-Sala, B. et al. A single-cell molecular map of mouse gastrulation and early organogenesis. *Nature* **566**, 490–495 (2019).
69. Li, W., Germain, R. N. & Gerner, M. Y. Multiplex, quantitative cellular analysis in large tissue volumes with clearing-enhanced 3D microscopy (Ce3D). *Proc. Natl Acad. Sci. USA* **114**, E7321–E7330 (2017).
70. Schindelin, J. et al. Fiji: an open-source platform for biological-image analysis. *Nat. Methods* **9**, 676–682 (2012).
71. Routy, B. et al. Gut microbiome influences efficacy of PD-1-based immunotherapy against epithelial tumors. *Science* **359**, 91–97 (2018).
72. Vetizou, M. et al. Anticancer immunotherapy by CTLA-4 blockade relies on the gut microbiota. *Science* **350**, 1079–1084 (2015).
73. Mielke, L. A. et al. TCF-1 limits the formation of Tc17 cells via repression of the MAF–RORγt axis. *J. Exp. Med.* **216**, 1682–1699 (2019).

Acknowledgements

We thank M. Camilleri, A. Lin, S. Cree, C. Alvarado and T. Putoczki for expert technical advice and support. We thank S. Wilcox for performing the sequencing, and S. Nutt for critical reading of the manuscript. Financial support for this work was provided by National Health and Medical Research Council (NHMRC) of Australia grants (APP1165443, 1122277 and 1054925 to G.T.B. and C.S.), Cure Cancer and Cancer Australia (APP1163990 to N.J.), The Rebecca L. Cooper Medical Research Foundation (to G.T.B.) and fellowships from the NHMRC (APP1135898 to G.T.B., APP1123000 to C.S. and APP1154970 to G.K.S.). This study was made possible through the Victorian State Government Operational Infrastructure Support Program and the Australian Government NHMRC Independent Research Institute Infrastructure Support Scheme.

Author contributions

C.S., K.L., A.L.G., P.H., N.J., J.T., V.C.W. and R.D.S. performed the experiments and data analyses. G.K.S., A.L.G., P.H. and M.E.R. oversaw the bioinformatic analyses. V.C.W., K.R. and L.W. oversaw the imaging analyses. G.T.B. wrote the draft manuscript and coedited it with C.S. and with the help of the other coauthors. G.T.B. and C.S. directed the studies.

Competing interests

The authors declare no competing interests.

Additional information

Extended data is available for this paper at https://doi.org/10.1038/s41590-019-0567-y.

Supplementary information is available for this paper at https://doi.org/10.1038/s41590-019-0567-y.

Correspondence and requests for materials should be addressed to C.S. or G.T.B.

Peer review information Ioana Visan was the primary editor on this article and managed its editorial process and peer review in collaboration with the rest of the editorial team.

Reprints and permissions information is available at www.nature.com/reprints.

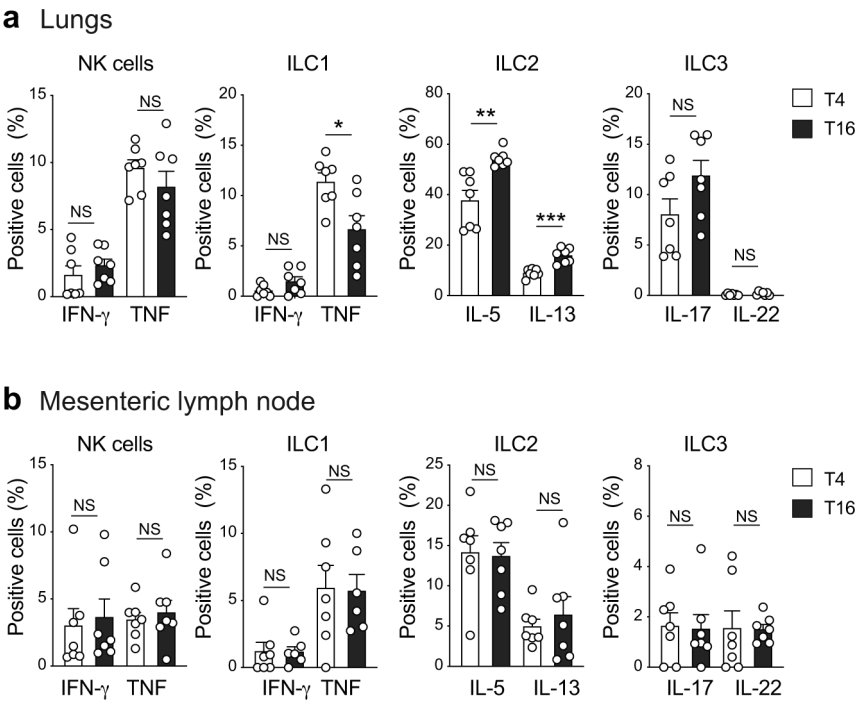

Extended Data Fig. 1 | Cytokine secretion of ILCs at T4 and T16. a,**b**, Frequency of cytokine-producing NK cells, ILC1, ILC2 and ILC3 isolated from the lungs (**a**) and mesenteric LN (**b**) at T4 and T16. IFN-γ, TNF-α, IL-5, IL-13, IL-17 and IL-22 production was determined by intracellular cytokine staining in the indicated populations. Individual responses together with mean ± s.e.m. are shown. **a**,**b**, $n = 7$ mice at each time point. Data is shown for one of four similar experiments for the lung analysis and six experiments for the mesenteric LN analysis. **a**,**b**, Statistical significance was determined using a two-tailed unpaired Student's t-test. *$P < 0.05$; **$P < 0.01$; NS, not significant.

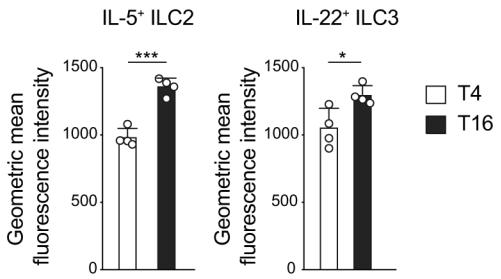

Extended Data Fig. 2 | Enhanced cytokine expression in ILC subsets at T4 and T16. Geometric mean fluorescence intensity of intracellular IL-5 and IL-22 cytokine production from ILC2 and ILC3, respectively, isolated from the small intestine of naïve C57BL/6 mice at T4 and T16. Shown are individual responses together with mean ± s.e.m. ($n = 4$ mice per time point) for one of four similar experiments. Statistical significance was determined using a two-tailed unpaired Student's *t*-test. *P < 0.05; **P < 0.01.

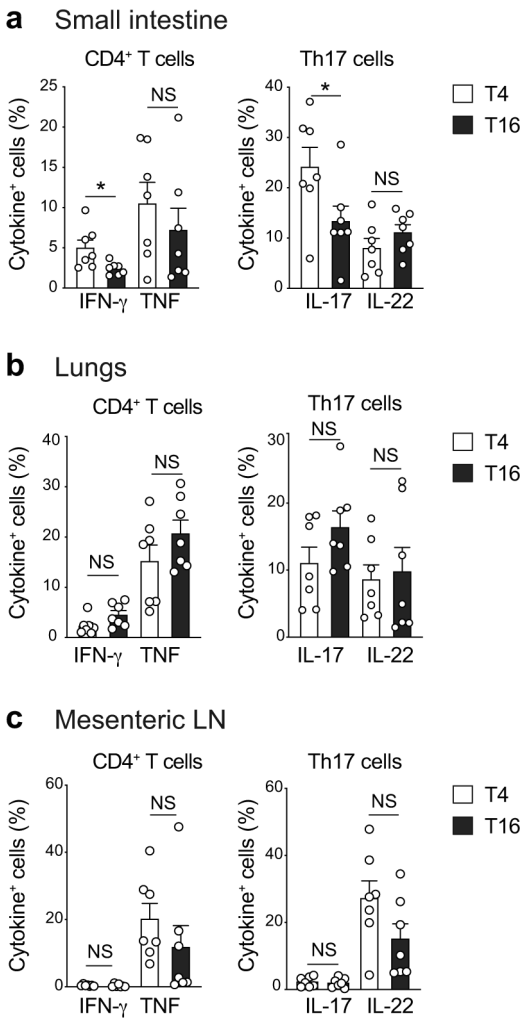

Extended Data Fig. 3 | Cytokine secretion of T lymphocytes at T4 and T16. a-c, Frequency of indicated cytokine produced by CD4$^+$ T cells and Th17$^+$ cells (CD4$^+$Rorγt$^+$) in the small intestine (**a**), lungs (**b**) and mesenteric LN (**c**) from naïve C57BL/6 mice at T4 and T16. IFN-γ, TNF-α, IL-17 and IL-22 production was determined by intracellular cytokine staining. Individual responses together with mean $\pm$ s.e.m. are shown. **a-c**, $n = 7$ mice at each time point. Data show one representative of four for the lung analysis, and one of six similar experiments for the small intestine and mesenteric LN analysis. **a**-**c**, Statistical significance was determined using a two-tailed unpaired Student's *t*-test. *P < 0.05; **P < 0.01; ***P < 0.001; NS, not significant.

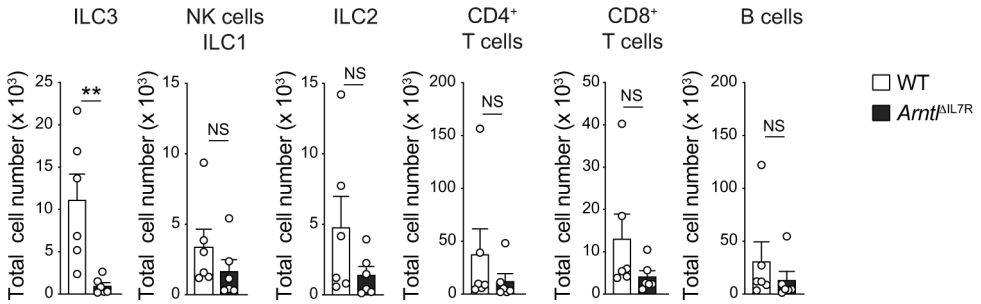

Extended Data Fig. 4 | Total number of lymphocytes in the small intestine of mixed bone-marrow chimeric mice. Mixed bone marrow chimeras were generated by reconstituting CD45.1$^{+/+}$ lethally irradiated recipients with a 1:1 proportion of F1 (CD45.1 × CD45.2, CD45.1^{+}CD45.2^{+}) wild-type and CD45.2$^{+/+}$ *Arntl*$^{\Delta IL-7R}$ bone marrow. Total number of different lymphocyte subsets isolated in the small intestine of mixed bone marrow chimeras are shown. Cells derived from wild-type (CD45.1^{+}CD45.2^{+}) bone marrow are indicated in white and cells from *Arntl*$^{\Delta IL-7R}$ (CD45.2$^{+/+}$) are shown in black. ILC subsets were gated as live lin^{-}(B220^{-}CD19^{-}CD3^{-}) CD45.1^{+}CD45.2^{+} (wild-type) or CD45.2$^{+/+}$ (*Arntl*$^{\Delta IL-7R}$) NK1.1^{+}NKp46^{+} NK cells/ILC1, NK1.1^{-}NKp46^{-}R orγt^{-}Gata3^{+} ILC2 and NK1.1^{-}NKp46$^{+/-}$ Rorγt^{+}Gata3^{-} ILC3. Data are representative of three independent experiments and show the mean ± s.e.m. for one experiment (n = 6 mice/experiment). Statistical significance was determined using a two-tailed unpaired Student's t-test. *P < 0.05; **P < 0.01.

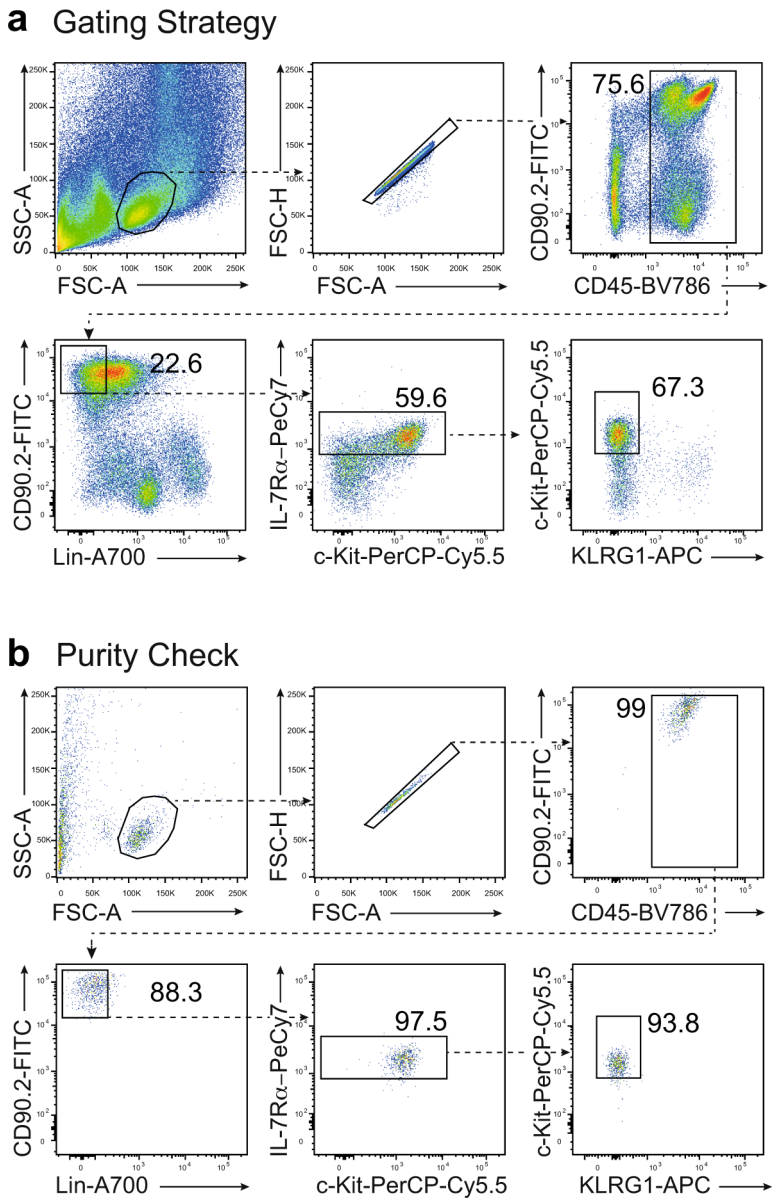

Extended Data Fig. 5 | Purification of small intestinal ILC3 from food-restricted mice. cytometric sorting of lin$^-$(CD3ε$^-$TCRβ$^-$CD19$^-$B220$^-$Gr1$^-$CD11b$^-$) CD45$^+$IL-7Rα$^+$CD90$^+$c-kit$^+$ KLRG1$^-$ cells using a BD FACSARIA III (BD Biosciences). **a**, Representative dot plots show the cell surface markers and gating strategy used to discriminate ILC3 from other ILC subsets. **b**, Representative analyses of ILC3 purity after cell sorting of 26 independent sorts.

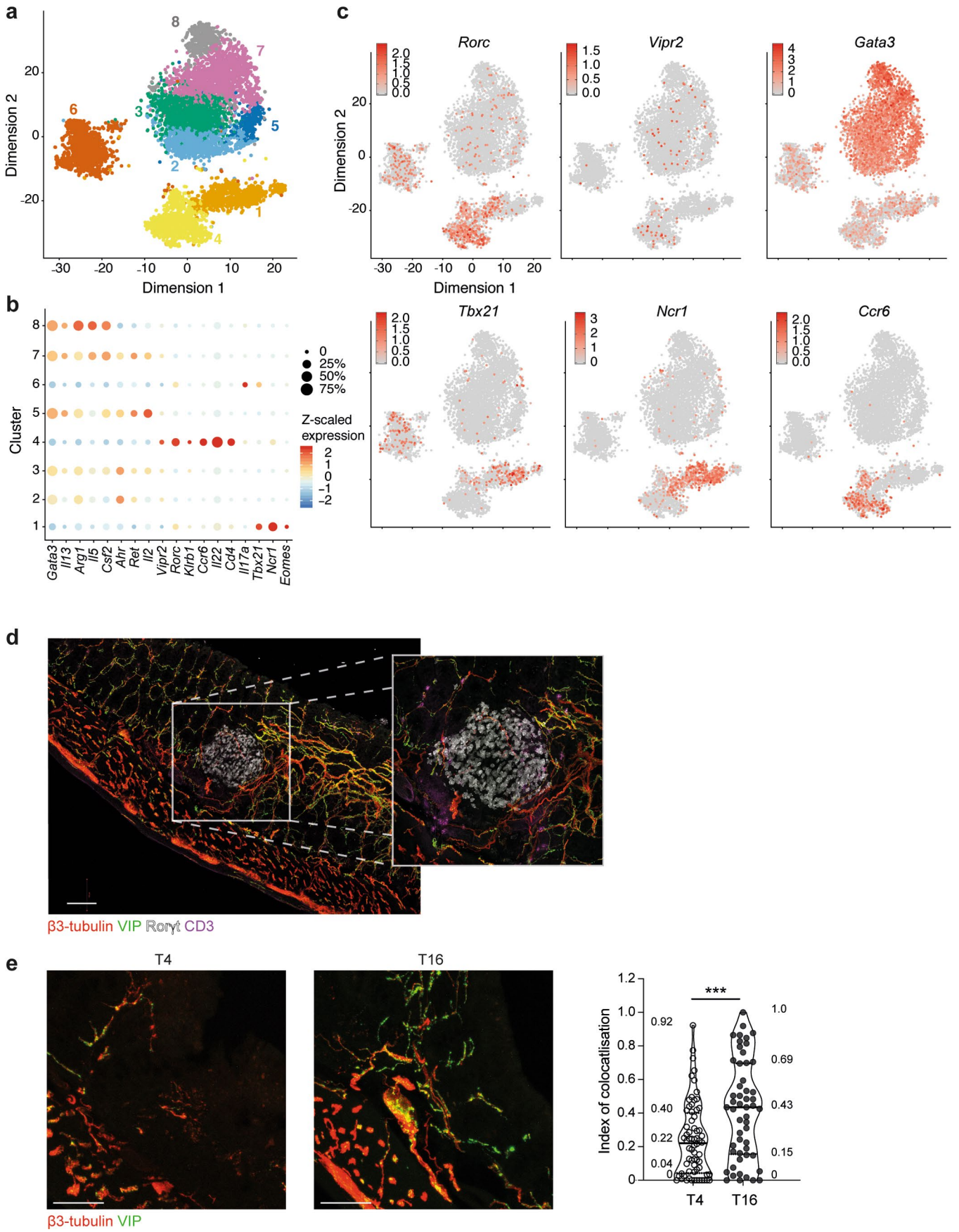

Extended Data Fig. 6 | See next page for caption.

Extended Data Fig. 6 | Single cell RNA-sequencing of colon ILC3. a-**c**, ILC from colon were sorted and single cells were sequenced using 10× Genomics. **a**, *t*-Distributed stochastic neighbour embedding (t-SNE) plots show 7,388 cells (dots) coloured by cluster. **b**, Level of expression of indicated genes within the t-SNE plots. **c**, Representative differentially expressed genes (x axis) by cluster (y axis). Dot size represents the fraction of cells within the cluster that express each gene. The colour intensity indicates the z-scaled expression of genes in cells within each cluster. **d**, Confocal image of a frozen section of the colon of a *Rorc(γt)*$^{GFP/+}$ mouse stained for neurons (β3-tubulin III, red), VIP (green), ILC3 (RORγt-GFP^{+}CD3ε^{-}, white) and T cells (CD3ε^{+}, purple). Image is representative of 2 independent experiments with 2 mice per experiment. Scale bar, 100 μm. **e**, Confocal images of frozen sections of colon from *Rorc(γt)*$^{GFP/+}$ mice at T4 (n = 68) and T16 (n = 53) stained for neurons (β3-tubulin, red) and VIP (green). Violin plots show the minima, 25% percentile, median, 75% percentile, and maxima for neuron axons in the colon from two mice with 6–8 sections per timepoint. Representative of two independent experiments ($n = 2$ mice per condition). Scale bar, 50 μm. **e**, Statistical significance was determined using a two-tailed unpaired Student's *t*-test. ***P < 0.001.

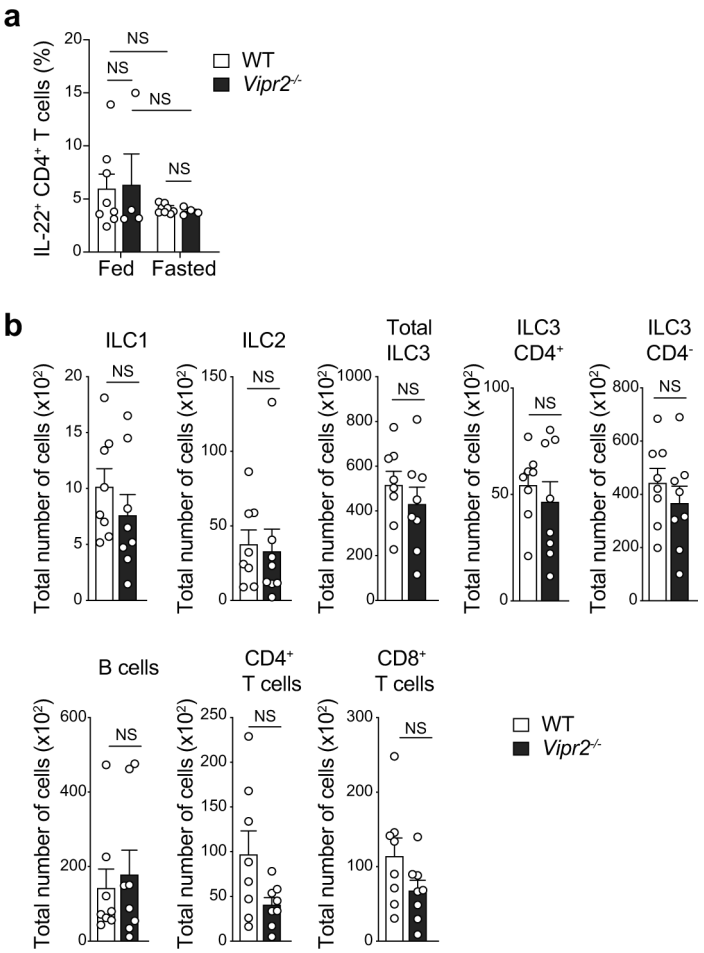

Extended Data Fig. 7 | Characterisation of lymphocytes in *Vipr2*$^{-/-}$mice. a, Wild-type and *Vipr2*$^{-/-}$ mice were fed *ad libitum* or fasted for 16 h and constitutive expression of IL-22 from CD4$^+$ T cells from the small intestine was determined by flow cytometry following 4 h *in vitro* culture. Data show the individual responses together with the mean ± s.e.m. pooled from two independent experiments ($n = 4$ Wild-type mice per experiment/condition and $n = 2$ *Vipr2*$^{-/-}$ mice per experiment/condition). **b**, Enumeration of ILC1, ILC2, total ILC3, CD4$^+$ ILC3, CD4$^-$ ILC3, B cells, CD8$^+$ T cells and CD4$^+$ T cells isolated from the small intestine of naïve wild-type and *Vipr2*$^{-/-}$ mice. Data show the mean ± s.e.m. of one of two similar experiments ($n = 8$ mice per time point per experiment). **a**,**b**, Statistical significance was determined using a two-tailed unpaired Student's *t*-test. *P < 0.05; **P < 0.01; NS, not significant.

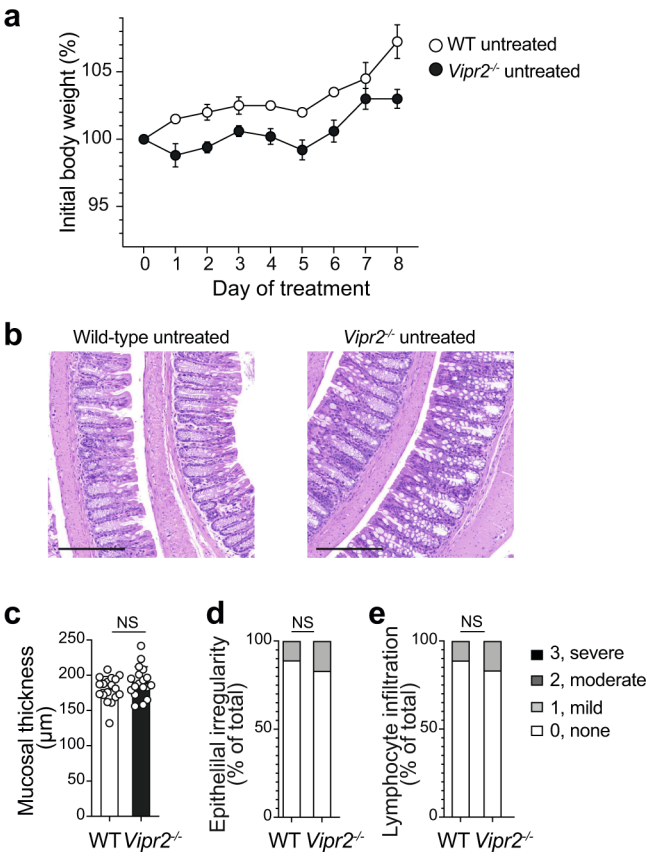

Extended Data Fig. 8 | Untreated *Vipr2*$^{-/-}$and wild-type mice maintain weight at steady-state. a, Weight changes for naive control wild-type and *Vipr2*$^{-/-}$ mice during the DSS treatment period shown in Fig. 7a. Data show mean ± s.e.m ($n = 5$ mice/genotype) percent of initial weight for one of two independent experiments with similar results. **b**, Representative H&E stained sections of the colon from untreated wild-type and *Vipr2*$^{-/-}$ mice. Scale bar, 200 µm. Images are representative of two independent experiments with similar results. **c-e**, Quantitative analysis of crypt height (**c**), epithelium irregularity (**d**) and inflammatory infiltrate (**e**) in untreated WT and *Vipr2*$^{-/-}$ mice. Epithelial length was measured in the distal part of the colon. Overall epithelial irregularity and inflammatory infiltrate was scored from six sections over two different slides per mouse (0 = normal, 1 = minor, 2 = moderate, 3 = severe). Mucosal thickness was measured across 12 randomly selected sites points per mouse. Data show mean ± s.e.m ($n = 3$ mice/genotype) of one of two independent experiments with similar results. **c-e**, Statistical significance was determined using a two-tailed unpaired Student's *t*-test. *P < 0.05; NS, not significant.

nature research

Corresponding author(s): Gabrielle T Belz and Cyril Seillet

Last updated by author(s): Nov 21, 2019

Reporting Summary

Nature Research wishes to improve the reproducibility of the work that we publish. This form provides structure for consistency and transparency in reporting. For further information on Nature Research policies, see Authors & Referees and the Editorial Policy Checklist.

Statistics

For all statistical analyses, confirm that the following items are present in the figure legend, table legend, main text, or Methods section.

n/a	Confirmed	
☐	☒	The exact sample size (*n*) for each experimental group/condition, given as a discrete number and unit of measurement
☐	☒	A statement on whether measurements were taken from distinct samples or whether the same sample was measured repeatedly
☐	☒	The statistical test(s) used AND whether they are one- or two-sided *Only common tests should be described solely by name; describe more complex techniques in the Methods section.*
☒	☐	A description of all covariates tested
☒	☐	A description of any assumptions or corrections, such as tests of normality and adjustment for multiple comparisons
☐	☒	A full description of the statistical parameters including central tendency (e.g. means) or other basic estimates (e.g. regression coefficient) AND variation (e.g. standard deviation) or associated estimates of uncertainty (e.g. confidence intervals)
☐	☒	For null hypothesis testing, the test statistic (e.g. *F*, *t*, *r*) with confidence intervals, effect sizes, degrees of freedom and *P* value noted *Give P values as exact values whenever suitable.*
☒	☐	For Bayesian analysis, information on the choice of priors and Markov chain Monte Carlo settings
☐	☒	For hierarchical and complex designs, identification of the appropriate level for tests and full reporting of outcomes
☒	☐	Estimates of effect sizes (e.g. Cohen's *d*, Pearson's *r*), indicating how they were calculated

Our web collection on statistics for biologists contains articles on many of the points above.

Software and code

Policy information about availability of computer code

Data collection	Aperio ImageScope v11.2.0.780, Zeiss LSM880 Confocal microscope, Zeiss Lightsheet Z.1, Illumina NextSeq platform.
Data analysis	Graphpad Prism 7.0 and 8.0, Imaris software v8 or 9, FlowJo v9, Zen software, FIJI (https://www.nature.com/articles/nmeth.2019); Bioconductor v3.9 (https://www.bioconductor.org/news/bioc_3_9_release/); simpleSingleCell workflow (http://bioconductor.org/packages/release/workflows/html/simpleSingleCell.html); DropletUtils package (vl.4.0; https://bioconductor.org/packages/release/bioc/html/DropletUtils.html); seater package (vl.12.2; https://bioconductor.org/packages/release/bioc/html/scater.html); Rtsne package (v0.13)(https://cran.r-project.org/web/packages/Rtsne); Reactome Pathway Analyses (https://reactome.org/); Rsubread package (v 1.26.1, https://bioconductor.org/packages/release/bioc/vignettes/Rsubread/inst/doc/Rsubread.pdf); Limma (v3.40.2; https://bioconductor.org/packages/release/bioc/html/limma.html); EdgeR (v3.26.5; https://bioconductor.org/packages/release/bioc/html/edgeR.html); RUV software package (v0.9.7; https://bioconductor.org/packages/release/bioc/html/RUVSeq.html); CRAN package pheatmap (v, 1.0.12, https://cran.r-project.org/web/packages/pheatmap/pheatmap.pdf); colocalization of VIP and ILC3 was determined using a custom written ImageJ macro to identify stained regions in sections then filter noise, thresholded and masked prior to analyses of pixel intensity.

For manuscripts utilizing custom algorithms or software that are central to the research but not yet described in published literature, software must be made available to editors/reviewers. We strongly encourage code deposition in a community repository (e.g. GitHub). See the Nature Research guidelines for submitting code & software for further information.

Data

Policy information about availability of data

All manuscripts must include a data availability statement. This statement should provide the following information, where applicable:

- Accession codes, unique identifiers, or web links for publicly available datasets
- A list of figures that have associated raw data
- A description of any restrictions on data availability

Raw data supporting the findings of this study are available from the corresponding authors on request.

Field-specific reporting

Please select the one below that is the best fit for your research. If you are not sure, read the appropriate sections before making your selection.

☒ Life sciences ☐ Behavioural & social sciences ☐ Ecological, evolutionary & environmental sciences

For a reference copy of the document with all sections, see nature.com/documents/nr-reporting-summary-flat.pdf

Life sciences study design

All studies must disclose on these points even when the disclosure is negative.

Sample size	Sample sizes were chosen based on prior research conducted in our laboratories to provide sufficient numbers of mice in each group to provide informative results and perform statistical testing, accounting for variability in possible cell isolation during the digestion process.
Data exclusions	No data was excluded from analysis.
Replication	Experiments were reliably reproduced and the number of experiments performed stated in methods and legends. Cumulated and pooled data is shown where possible. Where representative data is shown, relevant experiments were repeated successfully at least twice with the exact number of repeats indicated in each case. Most experiments were repeated at least twice if not three or more times to verify that experimental findings were reproducible.
Randomization	Animals of the same age and sex were randomly assigned to experimental groups.
Blinding	The analyses of DSS-induced pathology by histology was scored blindly according to the outlined criteria.

Reporting for specific materials, systems and methods

We require information from authors about some types of materials, experimental systems and methods used in many studies. Here, indicate whether each material, system or method listed is relevant to your study. If you are not sure if a list item applies to your research, read the appropriate section before selecting a response.

Materials & experimental systems

n/a	Involved in the study
☐	☒ Antibodies
☒	☐ Eukaryotic cell lines
☒	☐ Palaeontology
☐	☒ Animals and other organisms
☒	☐ Human research participants
☒	☐ Clinical data

Methods

n/a	Involved in the study
☒	☐ ChIP-seq
☐	☒ Flow cytometry
☒	☐ MRI-based neuroimaging

Antibodies

Antibodies used

Antibodies used are described below:
Antibody, Clone, Colour, Supplier (Catalogue#), (dilution):

Anti-mouse a4b7 DATK32 APC eBioscience 17588780, (1/300)

Anti-mouse c-Kit (CD117) 2B8 PerCP eFluor 710 eBioscience 46-1171-80 (1/200)

Anti-mouse CCR6 (CD196) 29-2L17 BV605 BioLegend 129819 (1/100)

Anti-mouse CDllb (Mac-1) Ml/70 ALEXA 700 WEHI Antibody Facility (1/400)

Anti-mouse CDllb (Mac-1) Ml/70 BV510 BD Horizon 562950 (1/800)
Anti-mouse CDllb (Mac-1) Ml/70 FITC BD Bioscience Pharmingen 553310 (1/200)
Anti-mouse CDllb (Mac-1) Ml/70 PB BD Horizon 560455 (1/500)

Anti-mouse CDllc HL3 APC BD Bioscience Pharmingen 550261 (1/100)
Anti-mouse CDllc HL3 PE eBioscience 553802 (1/200)
Anti-mouse CDllc HL3 PE-Cy7 BD Bioscience Pharmingen 2160675 (1/100)

Anti-mouse CD122 TM-bl BV650 BD OptiBuild 740475 (1/200)

Anti-mouse CD127 SB/199 PE Cy7 BD Bioscience Pharmigen 560733 (1/100)

Anti-mouse CD135 (Flt3) A2F10.1 PE BD Bioscience Pharmingen 553842 (1/100)

Anti-mouse CD19 103 ALEXA 700 WEHI Antibody Facility (1/400)
Anti-mouse CD19 eBiolD3 APC eFluor 780 eBioscience 47-0193-82 (1/800)
Anti-mouse CD19 103 BUV395 BD Horizon 563557 (1/800)
Anti-mouse CD19 103 BUV737 BD Horizon 564296 (1/400)
Anti-mouse CD19 103 PB WEHI Antibody Facility (1/100)
Anti-mouse CD19 103 PE-Cy7 BD Bioscience Pharmingen 552854 (1/1000)

Anti-mouse CD3e 145-2Cll ALEXA 700 WEHI Antibody Facility (1/400)
Anti-mouse CD3e 17A2 APC/Fire 750 Biolegend 100247 (1/300)
Anti-mouse CD3e 145-2Cll BUV395 BD Horizon 563565 (1/200)
Anti-mouse CD3e 145-2Cll eFluor450 eBioscience 48-0031-82 (1/100)

Anti-mouse CD4 GKl.5 APC-Cy7 BD Bioscience Pharmingen 561830 (1/1000)
Anti-mouse CD4 GKl.5 PE-Cy7 eBioscience 25-0041-82 (1/100)

Anti-mouse Pan-CD45 30-Fll BV786 BD Bioscience Pharmigen 564225 (1/1000)

Anti-mouse CD45.l A20 APC BD Bioscience Pharmingen 558701 (1/100)
Anti-mouse CD45.l A20 BV510 BD Horizon 565248 (1/400)
Anti-mouse CD45.l A20 BV650 BD Horizon 563754 (1/300)

Anti-mouse CD45.2 104 BV786 BD Bioscience Pharmingen 563686 (1/200)
Anti-mouse CD45.2 104 FITC BD Bioscience Pharmingen 553772 (1/1000)

Anti-mouse CD49a Ha31/8 BV711 BD Bioscience Pharmingen 563545 (1/100)

Anti-mouse CD49b (Integrin a2) DX5 ALEXA 594 WEHI Antibody Facility (1/300)
Anti-mouse CD49b (Integrin a2) DX5 PB WEHI Antibody Facility (1/200)

Anti-mouse CD90.2 (Thy 1.2) 30-H12 FITC WEHI Antibody Facility (1/1000)
Anti-mouse CD90.2 (Thy 1.2) 53-2.1 PB eBioscience 48-0902-82 (1/400)
Anti-mouse CD90.2 (Thy 1.2) 30-H12 PE BD Bioscience Pharmingen 553014 (1/800)

Anti-mouse EOMES Danl/mg eFluor 710 eBioscience 46487582 (1/400)

Anti-mouse GATA3 L50-823 BV711 BD Biosciences 565449 (1/300)
Anti-mouse GATA3 TWAJ PE eBioscience 12-9966-42 (1/200)
Anti-mouse GATA3 TWAJ PERCP 5.5 eBioscience 46996642 (1/200)

Anti-mouse IL-5 TRFK5 PE eBioscience 12705281(1/500)

Anti-mouse IL-13 EBio13A FITC eBioscience 11-9392-82 (1/200)

Anti-mouse IL-17A eBio17B7 PER CP 5.5 eBioscience 45-7177-82 (1/500)

Anti-mouse IL-22 IL22JOP, eBioscience 17-7222-80 (1/300)

Anti-mouse KLRGl 2Fl APC eBioscience 17-5893-81 (1/300)
Anti-mouse KLRGl 2Fl BV711 BD Horizon 564014 (1/400)

Anti-mouse Ly6C HKl.4 PER CP 5.5 eBioscience 45-5932-82 (1/400)

Anti-mouse Ly6G 1A8 BV510 BD OptiBuild 740157 (1/800)

Anti-mouse Ly6G/Ly6C (Gr-1) RB6-8C5 PE-Cy7 BD Bioscience Pharmingen 552985 (1/500)

Anti-mouse NKl.1 PK136 APC-Cy7 BD Bioscience Pharmingen 560618 (1/100)
Anti-mouse NKl.1 PK136 BV510 BD Horizon 563096 (1/400)
Anti-mouse NKl.1 PK136 BV650 BD Horizon 564143 (1/400)

Anti-mouse NKp46 (CD335) 29Al.4 PE eBioscience 12-3351-82 (1/100)

Anti-mouse NKp46 (CD335) 29Al.4 PE-Cy7 eBioscience 25-3351-82 (1/100)

Anti-mouse Rorgt Q31-378 BV421 BD Biosciences 562894 (1/300)

Anti-mouse Siglec-F E50-2440 PE BD Bioscience Pharmingen 552126 (1/800)

Anti-mouse ST2 (IL-33R) RMST2-2 eFluor 710 eBioscience 46933582 (1/200)

Anti-mouse TCRbeta H57-597 APC-Cy7 eBioscience 47-5961-82 (1/300)
Anti-mouse TCRbeta H57-597 PE-Cy7 BioLegend 109222 (1/400)

Anti-mouse TER119 TER-119 A700 WEHI Antibody Facility (1/200)

Validation

All antibodies were obtained from commercial vendors and we based specificity on descriptions and information provided in corresponding Data Sheets available and provided by the Manufacturers. All antibodies were validated and appropriate dilutions were determined by titration on ex vivo naive splenocytes or bone marrow cells.

Animals and other organisms

Policy information about studies involving animals; ARRIVE guidelines recommended for reporting animal research

Laboratory animals

Bmal1fl/fl (B6.129S4(Cg)-Arntltm1Weit/J), Il7rCre, Vipr2-/- (B6.129P2-Vipr2tm1Ajh/J) , Rag1-/- (B6.129S7-Rag1tm1Mom/J), Rag2-/-gammac-/- mice were maintained on a C57BL/6 (Ly5.2) background (all originally derived from the Jackson Laboratory) have been described previously. Bmal1fl/fl mice were crossed to the Il7rCre strain to generate the Bmal1fl/flIl7rCre line that lacks BMAL1 in all lymphocytes. C57BL/6, B6.SJL-PtprcaPep3b/BoyJ (Ly5.1+/+, CD45.1+/+) and Ly5.1+Ly5.2+(F1) mice were bred and maintained in-house. All mice were were used at 7-12 weeks old. Male and female mice were used at 8–14 weeks old, unless stated otherwise. In all experiment mice were Sex- and age-matched.

Wild animals

The study did not involve wild animals.

Field-collected samples

The study did not involve field-collected samples.

Ethics oversight

Animals were handled according to the guidelines of the Australian code for the care and use of animals of the National Health and Medical Research Council of Australia. Experimental procedures were approved by the Animal Ethics Committee of the Walter and Eliza Hall Institute of Medical Research.

Note that full information on the approval of the study protocol must also be provided in the manuscript.

Flow Cytometry

Plots

Confirm that:

☒ The axis labels state the marker and fluorochrome used (e.g. CD4-FITC).

☒ The axis scales are clearly visible. Include numbers along axes only for bottom left plot of group (a 'group' is an analysis of identical markers).

☒ All plots are contour plots with outliers or pseudocolor plots.

☒ A numerical value for number of cells or percentage (with statistics) is provided.

Methodology

Sample preparation

Sample preparation is described in the Materials & Methods section.

Instrument

FACS Canto II or Fortessa X20 (BD Biosciences) for flow cytometry; FACSAria III (BD Biosciences) for FACS sorting.

Software

FlowJo software 9 (Treestar)

Cell population abundance

Gating strategy and indicative frequencies/abundance of populations are provided in Supplementary Fig. 4.

Gating strategy

ILC3 were identified as CD45+CD90+CD117+IL-7Ralpha+NKp46+/- and negative for KLRG1, TER119, B220, CD19, CD3, TCRb, CD11b and NK1.1.

☒ Tick this box to confirm that a figure exemplifying the gating strategy is provided in the Supplementary Information.